https://doi.org/10.1093/plphys/kiac528 PLANT PHYSIOLOGY 2023: 191: 1574–1595

Plant Physiology®

Research Article

Plant lineage-specific PIKMIN1 drives APC/C^{CCS52A2} E3-ligase activity-dependent cell division

Alex Willems [1,2], Yuanke Liang [1,2], Jefri Heyman [1,2], Thomas Depuydt [1,2], Thomas Eekhout [1,2], Balkan Canher [1,2], Hilde Van den Daele [1,2], Ilse Vercauteren [1,2], Klaas Vandepoele [1,2] and Lieven De Veylder [1,2,*,†]

1 Department of Plant Biotechnology and Bioinformatics, Ghent University, Ghent B-9052, Belgium
2 Center for Plant Systems Biology, VIB, Ghent B-9052, Belgium

*Author for correspondence: lieven.deveylder@psb.vib-ugent.be (L.D.V.)
†Senior author.

A.W., K.V., and L.D.V. conceived and designed the experiments; A.W., Y.L., J.H., T.D., B.C., H.V.d.D., and I.V. performed the experiments; A.W., Y.L., T.E., T.D., and L.D.V. analyzed the data; A.W., Y.L., T.D., and L.D.V. wrote the manuscript.
The author responsible for distribution of materials integral to the findings presented in this article in accordance with the policy described in the Instructions for Authors (https://academic.oup.com/plphys/pages/General-Instructions) is: Lieven De Veylder (lieven.deveylder@psb.vib-ugent.be).

Abstract

The anaphase-promoting complex/cyclosome (APC/C) marks key cell cycle proteins for proteasomal breakdown, thereby ensuring unidirectional progression through the cell cycle. Its target recognition is temporally regulated by activating subunits, one of which is called CELL CYCLE SWITCH 52 A2 (CCS52A2). We sought to expand the knowledge on the APC/C by using the severe growth phenotypes of *CCS52A2*-deficient Arabidopsis (*Arabidopsis thaliana*) plants as a readout in a suppressor mutagenesis screen, resulting in the identification of the previously undescribed gene called *PIKMIN1* (*PKN1*). PKN1 deficiency rescues the disorganized root stem cell phenotype of the *ccs52a2-1* mutant, whereas an excess of PKN1 inhibits the growth of *ccs52a2-1* plants, indicating the need for control of PKN1 abundance for proper development. Accordingly, the lack of PKN1 in a wild-type background negatively impacts cell division, while its systemic overexpression promotes proliferation. PKN1 shows a cell cycle phase-dependent accumulation pattern, localizing to microtubular structures, including the preprophase band, the mitotic spindle, and the phragmoplast. PKN1 is conserved throughout the plant kingdom, with its function in cell division being evolutionarily conserved in the liverwort *Marchantia polymorpha*. Our data thus demonstrate that PKN1 represents a novel, plant-specific protein with a role in cell division that is likely proteolytically controlled by the CCS52A2-activated APC/C.

Introduction

The selective destruction of proteins is essential to provide unidirectionality and finality to cellular processes such as the cell cycle. One way to achieve this is through the ubiquitin-proteasome pathway. Ubiquitination is the process of attaching a ubiquitin moiety to a target protein, which results in its recognition and proteolytic destruction by the 26S proteasome (Glickman and Ciechanover, 2002). The process of ubiquitination involves a set of enzymatic reactions: an E1 ubiquitin-activating enzyme binds and activates the ubiquitin in an ATP-dependent manner, the activated ubiquitin is subsequently transferred to an E2 ubiquitin-conjugating enzyme, and finally, an E3 ubiquitin ligase catalyzes the transfer of ubiquitin from the E2 enzyme to a target protein (Hershko and Ciechanover, 1998). A particular E3 ligase involved in the progression of the cell cycle is the anaphase-promoting complex/cyclosome (APC/C, see Willems and De Veylder (2022) for an extensive review about the plant APC/C). The APC/C is a multi-subunit complex that is strongly conserved throughout eukaryotes, with its

Received August 10, 2022. Accepted November 18, 2022. Advance access publication November 24, 2022

core subunits named APC1 through APC16, of which only a few appear to be kingdom-specific (Eme et al., 2011).

APC/C substrate recognition and binding is provided by two co-activators, one being the core subunit APC10 and the other being a CELL DIVISION CYCLE 20/FIZZY (CDC20/FZ) or CDC20 HOMOLOGUE 1/FIZZY-RELATED (CDH1/FZR) WD-40 domain-containing protein (Tarayre et al., 2004; da Fonseca et al., 2011; Kevei et al., 2011; Zhou et al., 2016). These activator proteins recruit the APC/C-ubiquitination targets through recognition of conserved amino acid motifs called degrons, such as the Destruction box (D-box), with the consensus sequence RxxLxxxxN, or the KEN- or GxEN-boxes (Pfleger and Kirschner, 2000; De Veylder et al., 2007; Heyman and De Veylder, 2012).

The CDC20/FZ-type activator is present in six copies in Arabidopsis (*Arabidopsis thaliana*), of which only CDC20.1 and CDC20.2 are thought to be functional, whereas the CDH1/FZR-type, also known as CELL CYCLE SWITCH 52 (CCS52), is present in three copies, two A-types (*CCS52A1* and *CCS52A2*) and one B-type (*CCS52B*) (Tarayre et al., 2004; Kevei et al., 2011). Both *CDC20* genes and *CCS52B* show a similar cell cycle phase-dependent expression, peaking from the G2- to M-phase, whereas their protein levels are temporally controlled by nuclear mRNA sequestration until the breakdown of the nuclear envelope at the prometaphase, indicating that they both play a role in the progression of mitosis (Tarayre et al., 2004; Fülöp et al., 2005; Kevei et al., 2011; Yang et al., 2017). In contrast, both *CCS52A* isoforms are mainly expressed from the late M-phase to G2 (Kevei et al., 2011). Plants with a diminished activity of either CCS52A isoform show a reduction in leaf cell size, accompanied by a decrease in the DNA ploidy level, while the opposite holds true for plants overexpressing either isoform (Lammens et al., 2008; Boudolf et al., 2009; Larson-Rabin et al., 2009; Baloban et al., 2013; Heyman et al., 2017). Their only partially overlapping tissue-specific expression patterns hint to both isoforms performing specific functions (Baloban et al., 2013). Correspondingly, *ccs52a1* mutants show a reduction in trichome branch number and an increased cell number within their root meristem, while *ccs52a2* mutants show unprogrammed and aberrant cell divisions in the quiescent (QC) and organizing (OC) centers of, respectively, the root and the shoot meristems, accompanied by an overall dwarf growth, including a short root length and a strong reduction in the growth of inflorescences (Boudolf et al., 2009; Vanstraelen et al., 2009; Kasili et al., 2010; Liu et al., 2012; Heyman et al., 2017).

Although many plant proteins are assumed to be APC/C-ubiquitination targets, as the motifs necessary for their recognition by the APC/C are present in their amino acid sequence, only a limited set of APC/C substrates have been thoroughly characterized. Cyclins (CYCs), a family of proteins that, together with their cyclin-dependent kinase (CDK) binding partners, promote cell cycle progression through phosphorylation of target proteins, are known from research in animals and yeast to be genuine APC/C substrates (Peters, 2002). Various A- and B-type CYCs have also been shown to be targeted by the APC/C in plants, with evidence being most comprehensive for CYCA2;3 (Boudolf et al., 2009; Heyman et al., 2011; Eloy et al., 2012; Xu et al., 2016), CYCA3;4 (Fülöp et al., 2005; Willems et al., 2020), and CYCB1;1 (Kwee and Sundaresan, 2003; Fülöp et al., 2005; Rojas et al., 2009; Eloy et al., 2011; Zheng et al., 2011; Wang et al., 2012, 2013; Guo et al., 2016). Other cell division-related proteins characterized to be APC/C substrates include the cell wall biosynthesis gene CELLULOSE SYNTHASE LIKE-D 5 (CSLD5) (Gu et al., 2016), the rice (*Oryza sativa*) protein ROOT ARCHITECTURE ASSOCIATED 1 (RAA1, known as FLOWERING-PROMOTING FACTOR 1 [FPF1] in Arabidopsis) that interacts with the spindle and inhibits metaphase-to-anaphase transitions (Ge et al., 2004; Han et al., 2008; Xu et al., 2010), and the Arabidopsis PATRONUS1 (PANS1) and rice RICE SALT SENSITIVE 1 (RSS1) proteins that are essential for sister chromatid cohesion during the early stages of cell division (Ogawa et al., 2011; Cromer et al., 2013; Juraniec et al., 2016; Cromer et al., 2019). Several other proteins indirectly related to the cell division process have been implicated to be APC/C targets as well, including the DSRNA-BINDING PROTEIN 4 (DRB4) involved in RNA silencing (Marrocco et al., 2012), the transcription factor ETHYLENE RESPONSE FACTOR 115 (ERF115) that controls QC divisions in the root tip (Heyman et al., 2013), the rice transcription factor MONOCULM 1 (MOC1, called SCARECROW-LIKE 18/LATERAL SUPPRESSOR [SCL18/LAS] in Arabidopsis) involved in shoot branching (Lin et al., 2012, 2020; Xu et al., 2012), the rice homolog of the SHORT ROOT (OsSHR) transcription factor involved in root growth (Lin et al., 2020), the rice RCAR family of abscisic acid receptors (Lin et al., 2015), and the DDR-complex subunit DEFECTIVE IN MERISTEM SILENCING 3 (DMS3) involved in the silencing of transposable elements (Zhong et al., 2019).

In this work, we exploited the outspoken short root phenotype of *CCS52A2* knock-out plants to identify previously unknown APC/$C^{CCS52A2}$ targets through an ethyl methanesulfonate (EMS) suppressor screen. We show that one of the identified revertants encodes a previously undescribed plant lineage-specific cell cycle protein that plays a putative role in microtubule dynamics and is likely targeted for destruction by APC/$C^{CCS52A2}$.

Results

Identification of *pkn1* as a *ccs52a2-1* suppressor mutant

Compared with the wild type, the *ccs52a2-1* mutant shows a strong primary root growth inhibition phenotype, especially the first days following germination, with a partial recovery during later development, reaching a total root length of 36% of that of wild-type plants at 9 days after stratification (DAS; Figure 1, A, B, E, and F, Supplemental Figure 1A) (Vanstraelen et al., 2009; Heyman et al., 2013;

Willems et al., 2020). This short root phenotype was used to identify putative targets of the APC/$C^{CCS52A2}$ ubiquitin ligase complex through an EMS mutagenesis revertant screen. Out of 260 initially identified revertants, 33 were confirmed in the next generation. Among these, one revertant mutation, named *pikmin 1-1* (*pkn1-1*), yielded a partial recovery in root length (Figure 1C, Supplemental Figure 1A). Compared with the *ccs52a2-1* mutant, the *pkn1-1 ccs52a2-1* double mutant showed improved root growth over almost all measured time points, being most outspoken at younger stages and with no significant difference at 9 DAS, reaching a total root length of 69% of that of the wild-type (Figure 1, E and F).

As previously described, the strongly reduced root growth in the *ccs52a2-1* mutant is accompanied by a severely disorganized root apical meristem stem cell niche (SCN) (Vanstraelen et al., 2009; Willems et al., 2020), as visualized through the use of a *proWOX5:GFP-GUS* transcriptional reporter that predominantly marks the QC stem cells. In the *ccs52a2-1* background, *WOX5* expression was detected in an expanded area of the disorganized QC and SCN during early development (at 5 DAS), as well as in differentiated columella cells and higher up in the root (Figure 1, G and H; Supplemental Figure 1, B and C). At a later developmental stage (at 9 DAS), *WOX5* expression was confined to the SCN, coinciding with improved root growth and meristem organization (Figure 1, J and K). Compared with the *ccs52a2-1* mutant, the *pkn1-1 ccs52a2-1* double mutant showed a substantially improved meristem organization at 5 DAS, accompanied by the exclusive expression of *WOX5* in the SCN, but no obvious differences were observed at 9 DAS (Figure 1, I and L; Supplemental Figure 1D).

To map the kinetics of the observed phenotypes, we compared root meristem organization between *ccs52a2-1* and *pkn1-1 ccs52a2-1* following root radical emergence. At 2 DAS, no clear differences in stem cell organization were observed between the genotypes (Supplemental Figure 2, A and J), indicating that the *ccs52a2-1* stem cell division phenotype is initiated post-embryonically. Accordingly, at 3 DAS, the *ccs52a2-1* SCN was disorganized (Supplemental Figure 2, B and E), being more outspoken at 5 DAS (Supplemental Figure 2, C and F). Within the *pkn1-1 ccs52a2-1* double mutant, the disorganized phenotype was clearly partially suppressed (Supplemental Figure 2, J–L), indicating that the presence of PKN1 accounts in large part for the early stem cell division phenotypes of the *ccs52a2-1* mutant. Interestingly, when quantifying the number of cells in cross sections of 5 DAS meristems, no substantial difference was observed between the different genotypes (Supplemental Figure 3), indicating that the severe phenotype of the *ccs52a2-1* mutant might not be caused by an altered cell division rate, but rather by a problem with correct cell plate positioning. The suppression of this phenotype in the *pkn1-1 ccs52a2-1* mutant suggests that the aberrant cell plate positioning depends at least in part on PKN1 presence.

At 9 DAS, the root meristem length of the *ccs52a2-1* mutant was only 75% of that of the wild type, caused by a reduction in cell number, probably in reaction to the disorganized SCN, whereas the cell size remained the same (Figure 1F). In the *pkn1-1 ccs52a2-1* double mutant, meristem length and cell number did not show improvement compared with the single *ccs52a2-1* mutant (Figure 1F), reflecting their similar root growth rates at 9 DAS (Figure 1E). Thus it appears that the root growth rescuing effect of the *pkn1-1* is confined to 3-to-8 DAS, probably by correcting the aberrant root meristem divisions observed in the *ccs52a2-1* mutant.

For the shoot tissue, recovery of the *ccs52a2-1* phenotype was detected for some but not all analyzed parameters at 21 DAS (Figure 1M). No difference in projected rosette size could be observed between *ccs52a2-1* and the double mutant, with both reaching only 58% and 61% of wild-type size, respectively (Figure 1M). Partial recovery was observed, however, for the size of the first leaf pair, with a reduction seen in *ccs52a2-1* to 48% and in the double mutant to 72% of the wild-type leaf size (Figure 1M). The leaf growth recovery phenotype appeared to be mostly driven by a recovery in cell number, with *ccs52a2-1* showing a reduction to 64% and *pkn1-1 ccs52a2-1* to 86% of the wild-type epidermal cell number (Figure 1M) and no significant difference in epidermal cell size, with a reduction for *ccs52a2-1* and *pkn1-1 ccs52a2-1* to 77% and 82% of the wild type, respectively (Figure 1M). Compared with the wild type, the reduction in the number of stomata per pavement cell (stomatal index or SI) was slightly greater in the *ccs52a2-1* mutant, with that of the double mutant being intermediate, although the differences were only minor (Figure 1M). DNA ploidy levels, as represented by the endoreplication index (EI), were reduced in the *ccs52a2-1* mutant to 78% of the wild type. In contrast, a partial or full recovery in the EI could be observed in the *pkn1 ccs52a2-1* double mutants (Figure 1M).

Identification of the *pkn1* mutant gene

To identify the gene underlying the *pkn1-1* mutation, a mapping scheme was set up wherein the *pkn1-1 ccs52a2-1* mutant was backcrossed with the original *ccs52a2-1* parental line and subsequently self-pollinated. In the resulting 1-in-4 segregating F2 mapping population, plants with the revertant phenotype were selected and pooled for gene mapping through next-generation sequencing, using the EMS-generated single-nucleotide polymorphisms (SNPs) as de novo mapping markers. Plotting the mutant allele frequency (the ratio of the number of mutant alleles over the number of wild-type alleles, also known as concordance) of the identified EMS-specific SNPs in function of their location in the genome revealed a peak at the end of chromosome 2 and subsequently, an interval was selected for detailed analysis (from 17 Mbp up to the end of chromosome 2, Supplemental Figure 4). After filtering for mutations with a concordance above 0.8 and filtering out intergenic or intronic mutations, four candidate genes were retained:

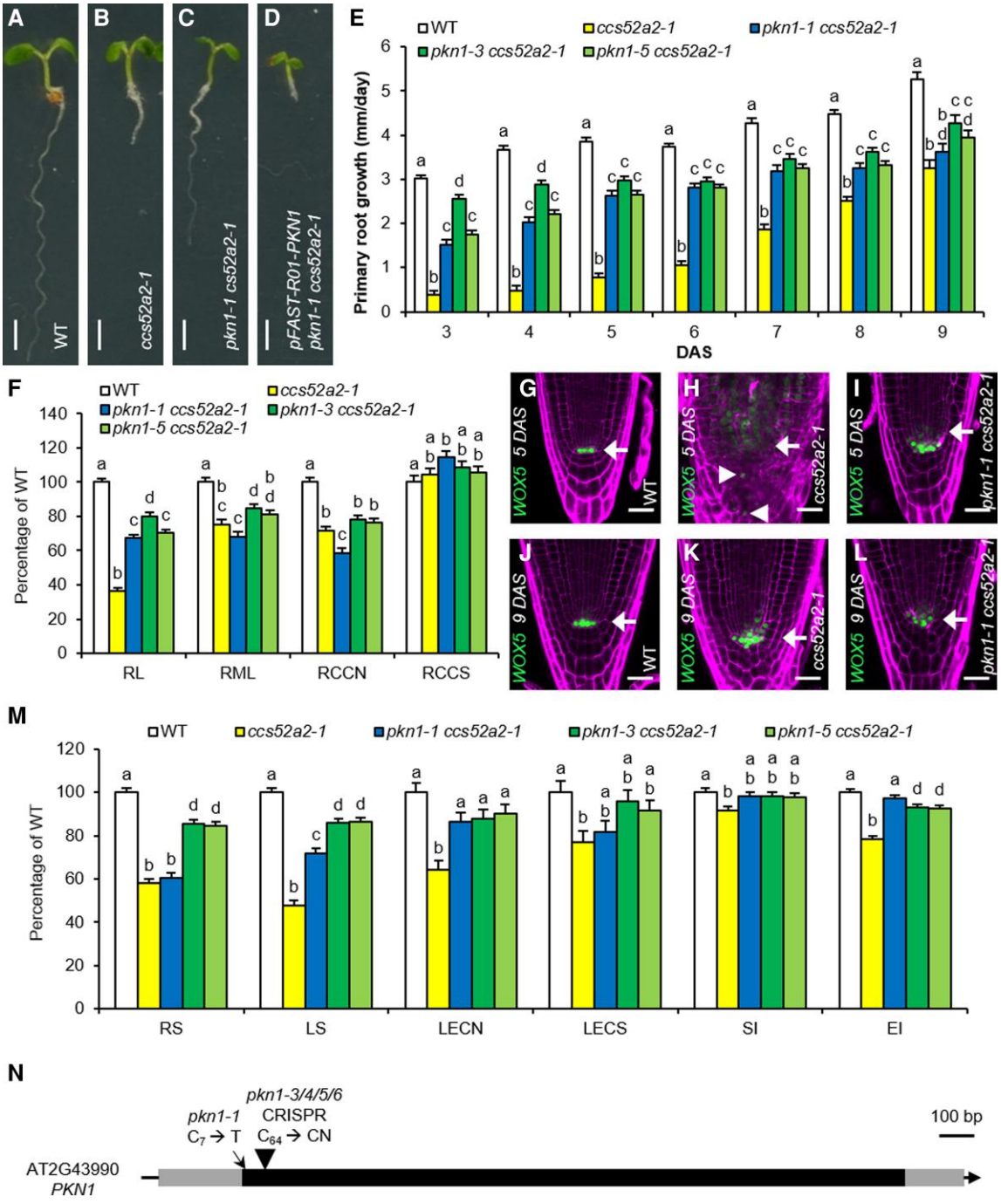

Figure 1 The *pkn1-1* mutation rescues the *ccs52a2-1* short root phenotype. A–D, Representative seedlings of the wild type (WT) (A), *ccs52a2-1* (B) and *pkn1-1 ccs52a2-1* without (C) and with (D) the *pFAST-R01-PKN1* complementation construct at 5 days after stratification (DAS). Scale bars represent 1 mm. E, F, and M, Growth characteristics of WT, *ccs52a2-1* and the double mutants *pkn1-1 ccs52a2-1*, *pkn1-3 ccs52a2-1* and *pkn1-5 ccs52a2-1*. Primary root growth from 3 to 9 DAS (E). Phenotypes of the primary root at 9 DAS (F). RL, root length; RML, root meristem length; RCCN, root cortical cell number; RCCS, root cortical cell size. Phenotypes of the shoot and the first leaf pair at 21 DAS (M). RS, rosette size; LS, leaf size; LECN, leaf epidermal cell number; LECS, leaf epidermal cell size; SI, stomatal index; EI, endoreplication index. Error bars represent standard error ($n \geq 9$). Letters on the bars indicate statistically different means ($P < 0.05$, mixed model analysis, Tukey correction for multiple testing). G–L, Representative confocal images of *proWOX5:GFP-GUS* expressing WT (G and J), *ccs52a2-1* (H and K) and *pkn1-1 ccs52a2-1* (I and L) primary root tips at 5 (G–I) and 9 DAS (J–L). Cell walls are visualized through propidium iodide staining. Arrows indicate the position of the QC, while ectopic *WOX5* expression in *ccs52a2-1* is indicated by arrowheads. Scale bars represent 25 µm. (*N*) The gene structure of the *PKN1* gene (*AT2G43990*), made up of a single exon, showing the location of the EMS mutation (arrow) and CRISPR mutations (small arrowhead). The gray and black boxes represent the untranslated regions and the coding sequence, respectively, while the lines represent intergenic sequences.

AT2G43190, *AT2G43990*, *AT2G45360*, and *AT2G46850* (Supplemental Table 1).

To investigate a potential link between any of the four high-concordance genes and the cell cycle, a co-expression analysis was carried out in which their transcriptome profile was compared with that of known cell cycle-related genes, over 18 different RNA-sequencing (RNA-seq) data sets (Depuydt and Vandepoele, 2021). For *AT2G43990*, the Gene Ontology (GO) term "cell division" (GO:0051301) was significantly overrepresented among its closely co-expressed genes in a root-specific network (GO:0051301 annotated to 27 co-expressed genes; Fisher's exact *P*-value < 10^{-10}; Supplemental Table 2), providing an indication that the causal mutation might be situated within the *AT2G43990* locus. Moreover, among its co-expressed genes, *CSLD5*, encoding a previously identified APC/$C^{CCS52A2}$ target, could be identified (Supplemental Table 3) (Gu et al. 2016). On top of the predicted role in cell division, the co-expression analysis similarly predicted *AT2G43990* to be involved in microtubule cytoskeleton organization (GO:0000226 annotated to 18 co-expressed genes; Fisher's exact *P*-value < 10^{-10}; Supplemental Table 2). In summary, these results provide evidence for a role of *AT2G43990* in cell division in roots, and a potential association with the microtubule array, therefore pointing towards *AT2G43990* as being the *pkn1-1* mutant gene.

To provide evidence for this putative association, we aimed at pinpointing the causative mutation by SNP-genotyping PCRs. In this analysis, the *AT2G43190* gene, encoding a subunit of the ribonuclease *P* complex involved in rRNA maturation (Gutmann et al., 2012), was not taken along, because it was deemed unlikely to play a role in *ccs52a2-1* phenotype recovery. SNP-genotyping PCR for the three remaining candidate mutations was performed on 133 plants with the long root phenotype from the segregating population used in the mapping of *pkn1-1 ccs52a2-1*. In this way, two plants could be isolated that were homozygous for the mutation in *AT2G43990* but contained a wild-type allele for *AT2G46850* or *AT2G45360*, indicating that the mutation in either of the latter two genes was unlikely to be responsible for the recovery phenotype. This was confirmed in the next generation, where all progeny of both plants showed the long root phenotype, and while the wild-type allele of *AT2G43990* could not be detected, the mutation in *AT2G45360* was found to be segregating in one population, while that in *AT2G46850* was segregating in both. This proved that the revertant phenotype is not associated with the EMS mutation in either *AT2G45360* or *AT2G46850*, ruling them out and leaving *AT2G43990* as the primary candidate for the actual revertant gene. As *AT2G43990* is an unknown gene and had not been named previously, it was chosen to keep the name *PIKMIN1* (*PKN1*). The *PKN1* gene consists of a single 1899-bp exon, with the EMS mutation (C_7→T) changing the third codon from one encoding arginine (CGA) to a STOP codon (TGA) (Figure 1N, Supplemental Table 1). Furthermore, the first few subsequent ATG codons, representing alternative starting points for translation initiation, are out-of-frame, strongly indicating that the EMS mutation represents a complete knock-out of the *PKN1* gene.

Transformation of a complementation construct containing a functional copy of the *PKN1* promoter and gene (*pFAST-R01-PKN1*) into the *pkn1-1 ccs52a2-1* mutant confirmed that the *pkn1-1* mutation in *AT2G43990* was responsible for the recovery of the *ccs52a2-1* root growth phenotype, as out of the 171 transformants obtained, 168 again showed a stunted root growth phenotype (Figure 1D). Remarkably, many transformants grew worse than *ccs52a2-1* plants, indicating that the growth phenotype of the *ccs52a2-1* plants strongly depends on PKN1 abundance and that timely breakdown of PKN1 might be essential for proper plant development.

PKN1 is an embryophyte-specific gene present as a single copy in most plant species

A search for potential homologs did not identify any closely related genes in Arabidopsis. In fact, *PKN1* appears to be a single-copy gene in most plant species (Supplemental Dataset 1), as can be deduced using the Dicot PLAZA 4.5 database for comparative plant genomics (Van Bel et al., 2018). BlastP searches further yielded potential *PKN1* homologs within the lycophyte lineage, represented by *Selaginella moellendorffii*, the liverwort lineage, represented by *Marchantia polymorpha*, and the moss lineage, represented by *Physcomitrium patens* (Supplemental Dataset 1). No *PKN1* homologs could be identified outside of the embryophyte clade, indicating that *PKN1* is likely a land plant-specific gene.

As no domain of the known function is present in any PKN1 homolog, the MEME suite (https://meme-suite.org/) was used to identify amino acid motifs conserved throughout the likely PKN1 homologs. Among the ten best computationally identified conserved motifs, of which motifs 1–8 are present in Arabidopsis PKN1 (AtPKN1), none had an annotated function (Figure 2). Among all investigated species, only motifs 3–5 are conserved, with motif 5 having a minimal D-box sequence (RxxL, Figure 2, Supplemental Figure 5). Within AtPKN1, a KGIL rather than the RxxL sequence is present in motif 5. Previous reports have shown that it is possible for a KxxL motif to insert in the binding pocket of APC/C (He et al., 2013; Qin et al., 2016), suggesting the KGIL in AtPKN1 motif 5 might still be recognized by the APC/C. Interestingly, all PKN1 sequences hold multiple putative APC/C recognition motifs (D-, KEN and GxEN-boxes), with a search using the Proviz tool (http://slim.icr.ac.uk/proviz/) additionally identifying a potential ABBA-motif in AtPKN1 (P^{389}MDIYKE), indirectly suggesting that PKN1 might be a bona fide APC/C target (Figure 2). Additionally, conserved Ser-Pro (SP) or Thr-Pro (TP) can be seen in motifs 3, 6, 7, and 8 (Supplemental Figure 5), representing potential sites for phosphorylation by CDKs or mitogen-activated protein kinases. In conclusion, the amino acid sequence analysis hints

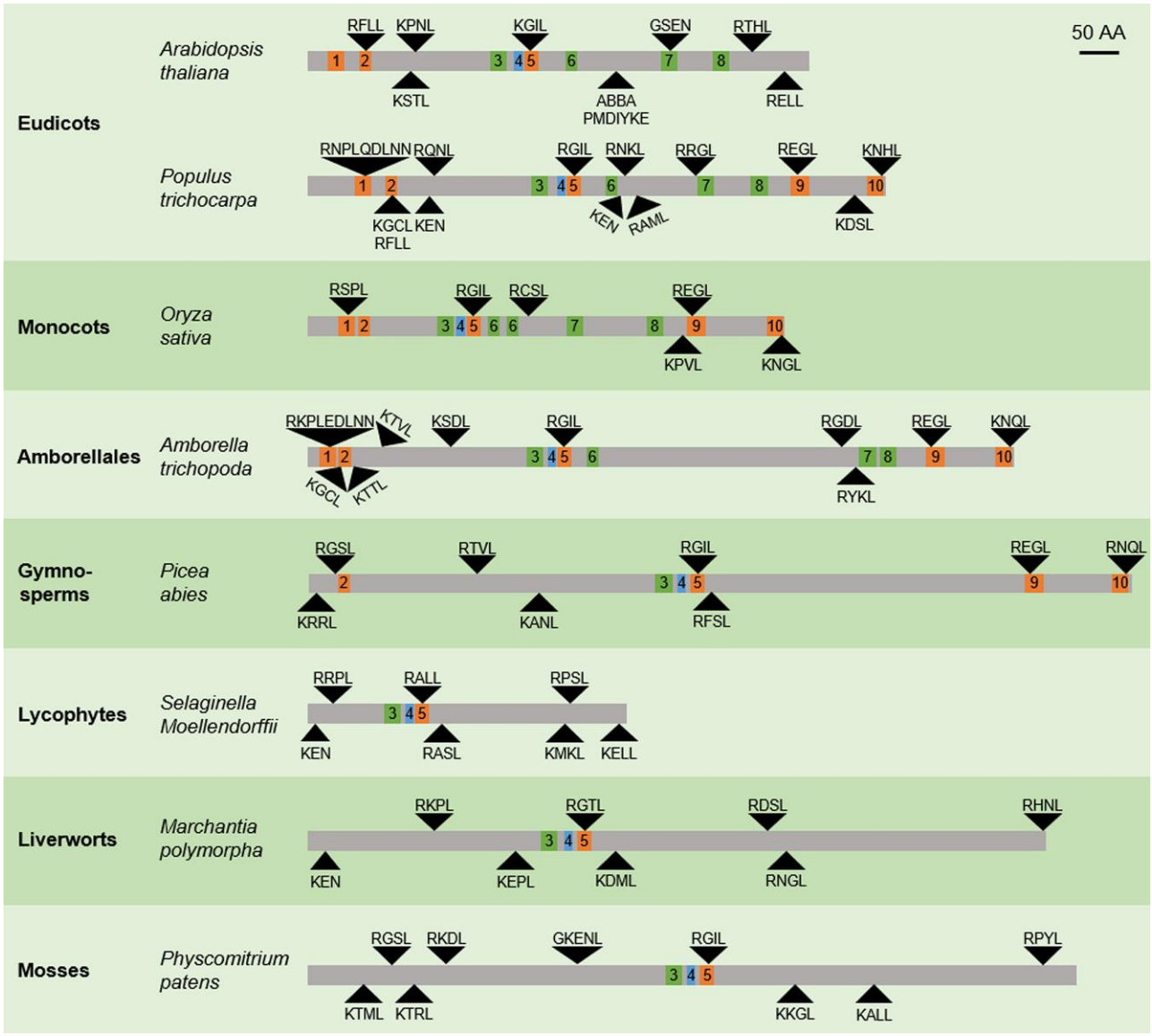

Figure 2 Conserved motifs in the PKN1 protein. The *Arabidopsis thaliana* PKN1 protein and its homologs throughout the plant kingdom, showing the location of the different conserved motifs identified (colored boxes) and of the D-box (showing both RxxL and KxxL sequences), KEN- or GxEN-boxes (black triangles). Motifs corresponding with a D-box are shown in orange, those corresponding with a possible phosphorylation site in green, and those without clear function in blue.

at PKN1 being a conserved protein that is potentially regulated in a cell cycle-dependent manner through ubiquitination by the APC/C and phosphorylation.

PKN1 is rate-limiting for cell division in the root meristem

To determine the effects of the lack of PKN1 on plant development, the *ccs52a2-1* mutation was crossed out of the *pkn1-1 ccs52a2-1* double mutant using Col-0, creating the *pkn1-1* single mutant. Although the root length of *pkn1-1* did not differ from that of the wild at 9 DAS, the root meristem length was reduced by 32%, and the root meristem cortical cell number was reduced by 39%, compensated by a small 13% increase in root cortical cell size (Figure 3A). No clear defects in root meristem organization could be observed (Supplemental Figure 2). On the level of the shoot, no significant differences could be observed for any of the investigated characteristics, except for a minor 10% increase in mature leaf size (Figure 3A).

To confirm the *pkn1-1* phenotypes, independent *PKN1* mutant lines were generated using the CRISPR/Cas9 technology. Two different guide RNAs were cloned into the same vector, with the expected cut sites in the beginning of the gene, after respectively base pair 64 and 286 of the *PKN1* CDS. For each of the six different T1 primary transformants,

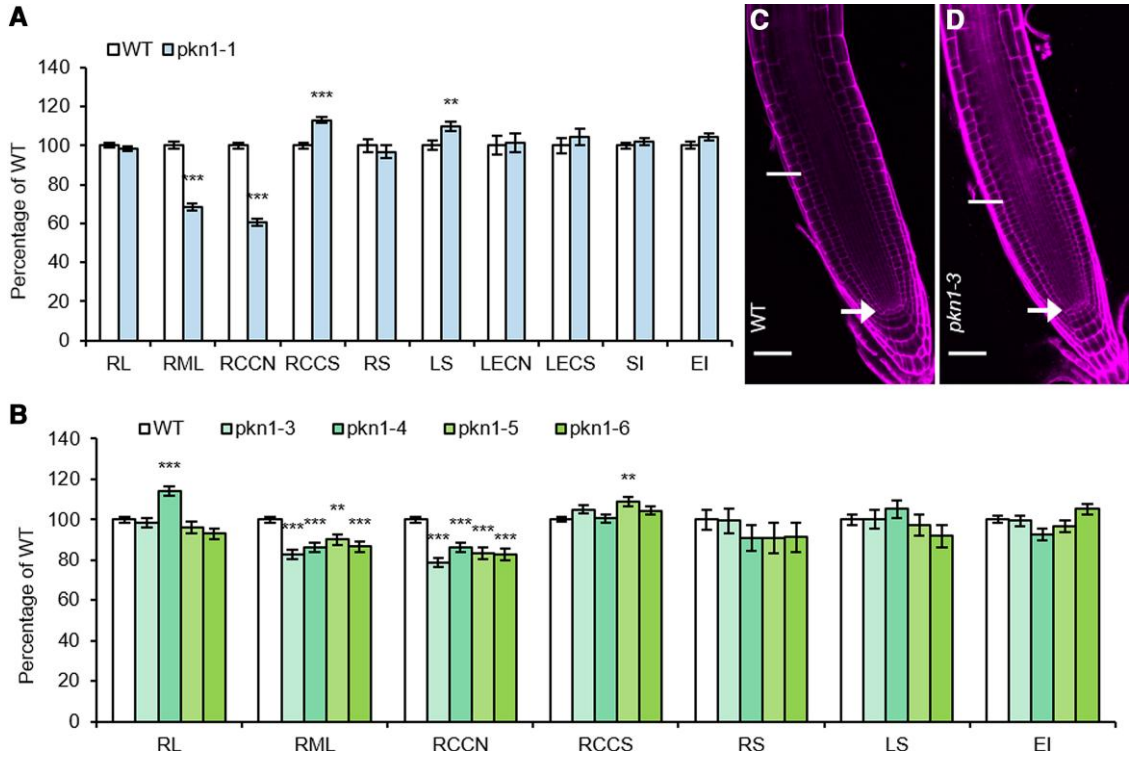

Figure 3 Characteristics of *pkn1* knock-out mutants. A, Phenotypes of the *pkn1-1* mutant in the root at 9 DAS and the shoot at 21 DAS; RL: root length ($n > 34$), RML: root meristem length ($n > 29$), RCCN: root cortical cell number ($n > 29$), RCCS: root cortical cell size ($n > 29$), RS: rosette size ($n > 38$), LS: leaf size ($n = 38$), LECN: leaf epidermal cell number ($n = 10$), LECS: leaf epidermal cell size ($n = 10$), SI: stomatal index ($n = 10$), EI: endoreplication index ($n = 10$). Error bars represent standard error and asterisks represent means significantly different from the wild-type (WT) mean (Mixed model analysis, ** $P < 0.01$, *** $P < 0.001$). B, Phenotypes of the *pkn1-3*, *pkn1-4*, *pkn1-5* and *pkn1-6* CRISPR mutants in the root at 9 DAS and the shoot at 21 DAS; RL ($n > 24$), RML ($n > 17$), RCCN ($n > 17$), RCCS ($n > 17$), RS ($n > 11$), LS ($n = 11$), EI ($n = 6$). Error bars represent standard error and asterisks represent means significantly different from the WT mean (Mixed model analysis with Dunnett correction for multiple testing, ** $P < 0.01$, *** $P < 0.001$). C and D, Representative confocal images of root tips of WT and the CRISPR mutant line *pkn1-3* at 9 DAS, highlighting the reduction in root meristem length in the mutant. Arrows and lines indicate the QC and the end of the proliferation zone, respectively. Scale bars represent 50 µm. Cell walls are visualized through propidium iodide staining.

seven to eight plants without the CRISPR/Cas9 construct were selected in the segregating T2 generation and screened for mutations at the two cut sites using SNP genotyping. Subsequently, the presence and the exact nature of the mutations were determined by Sanger sequencing, showing that editing at the first cut site was highly efficient, with many single-base pair INDELs, but no mutations at the second cut site. Some of the screened plants were already homozygous, and of those, four were retained: *pkn1-3* (insertion of T), *pkn1-4* (insertion of T), *pkn1-5* (insertion of C), and *pkn1-6* (insertion of A). In each case, the insertion behind C^{64} resulted in a frameshift and premature stop after six codons, most likely leading to a complete abolishment of the PKN1 function (Figure 1N).

Identical to the *pkn1-1* mutant line, root length at 9 DAS was not significantly different for all the CRISPR lines but *pkn1-4*, while root meristem length was reduced in all lines by 10%–18% compared with the wild type, caused by a reduction in cell number by 14%–21% (Figure 3, B–D). However, a large cell size increase, reminiscent to that of *pkn1-1*, could not be seen (Figure 3B). Like the *pkn1-1* mutant, no difference compared with the wild type was observed for the *PKN1* CRISPR mutants regarding any of the leaf parameters tested at 21 DAS, including rosette size, size of the first leaf pair, and ploidy levels (Figure 3B). Two of the CRISPR mutants, *pkn1-3* and *pkn1-5*, were introgressed into the *ccs52a2-1* background, and both double mutants showed an equal or better recovery of the *ccs52a2-1* phenotypes compared with *pkn1-1 ccs52a2-1*, confirming *PKN1* again as the true revertant gene (Figure 1, E, F and M).

Systemic *PKN1* overexpression promotes cell division in the leaf

To further investigate the potential role of PKN1 in cell division, *PKN1* overexpression lines ($PKN1^{OE}$) were generated by expressing the *PKN1*-coding sequence using the strong *Cauliflower Mosaic Virus 35S* (*CaMV 35S*) promoter. Overexpression levels of *PKN1* were measured in young

rosettes (10 DAS) of homozygous T3 lines and ranged between 4 and 90 times that of the wild type (Supplemental Figure 6A). For five of those lines, *PKN1* expression levels were also measured in the root tip and were found to range between 5 and 16 times that of the wild type (Supplemental Figure 6B). For phenotypical analysis, three lines were chosen with low (line 10.5), medium (line 7.6), and high (line 12.4) *PKN1* overexpression levels. In the shoot, all three lines showed an increased rosette size, with that of the high-overexpressing line being 19% larger than that of the wild type (Figure 4, A and C). This was reflected in the first leaf pair, with that of the medium line being 12% and that of the high line 17% larger than that of the wild type (Figure 4A). This increase in leaf size was caused by an increase in cell number, with the leaf epidermal cell number being increased between 10% and 17% for the three lines, while no difference was found for epidermal cell size (Figure 4A). Interestingly, this increase in cell number was mostly restricted to the stomata for the low and medium line, while the high line showed a similar increase in both stomata and pavement cells, leading to a higher SI for the low and medium lines, but not for the high line (Figure 4A). Additionally, the EI was not different compared with the wild-type (Figure 4A). In the root, *PKN1* overexpression did not affect growth, although a small, but significant, increase in root length was seen for the low and high line, accompanied by a small, but not statistically significant, increase in root meristem length and cell number (Figure 4B). The fact that the impact of increased PKN1 levels on cell number is mostly observed in the shoot might be due to an already higher level of PKN1 in the root tip than in the shoot in the wild-type plants (Supplemental Figure 6C).

PKN1 localizes at microtubular structures

To further investigate the possible function of the PKN1 protein, a GUS translational reporter construct (*proPKN1:PKN1-GUS*) was made. The PKN1 protein appeared to accumulate in dividing tissues throughout the plant, including the shoot and root apical meristems, the lateral and adventitious root initiation sites, the developing young leaves, the stomata, the trichome socket cells, the ovary, and the developing embryo (Figure 5, A–H). These tissue-specific accumulation patterns corroborate the idea that PKN1 plays a role in cell division.

To investigate the intracellular PKN1 localization pattern, GFP translational reporter constructs were generated. One construct, *pro35S:PKN1-GFP*, expressing *PKN1-GFP* under the control of the *CaMV 35S* promoter, was transiently

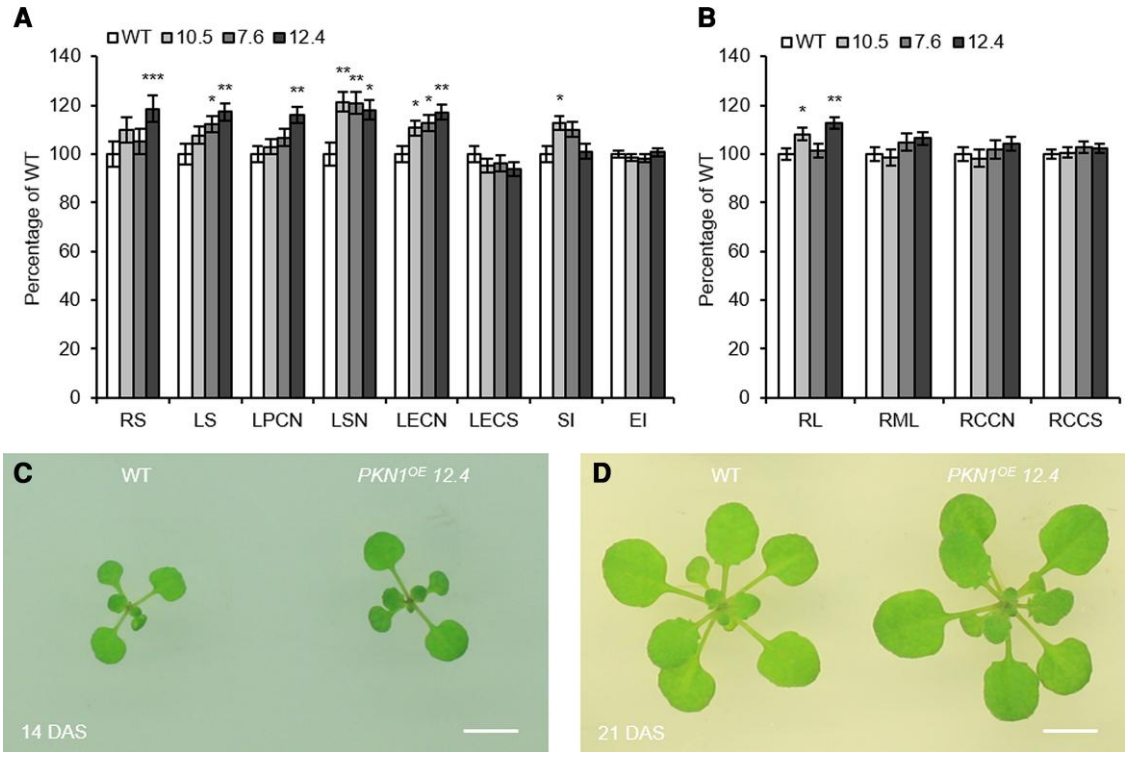

Figure 4 Overexpression of *PKN1*. A and B, Characteristics of the *PKN1*^{OE} lines in the shoot at 21 DAS (A) and the root at 9 DAS (B). RS: Rosette size ($n > 11$), LS: leaf size ($n > 10$), LPCN: leaf pavement cell number ($n = 10$), LSN: leaf stomatal number ($n = 10$), LECN: leaf epidermal cell number ($n = 10$), LECS: leaf epidermal cell size ($n = 10$), SI: stomatal index ($n = 10$), EI: endoreplication index ($n = 5$), RL: root length ($n > 13$), RML: root meristem length ($n > 10$), RCCN: root cortical cell number ($n > 10$), RCCS: root cortical cell size ($n > 10$). Error bars represent standard error and asterisks represent means significantly different from the wild-type (WT) mean (ANOVA with Dunnett correction for multiple testing, * $P < 0.05$, ** $P < 0.01$, *** $P < 0.001$). C and D, Representative images of rosettes of WT and *PKN1*^{OE} line 12.4 at 14 DAS (C) and 21 DAS (D), highlighting the increase in rosette size in the overexpressing line. Scale bars represent 0.5 cm.

transformed into *Nicotiana benthamiana* leaves through agroinfiltration, while two others, *proPKN1:PKN1-GFP* and *pro35S:GFP-PKN1*, expressing the PKN1-GFP or the GFP-PKN1 fusion under the control of its native promoter or the *CaMV 35S* promoter, respectively, were stably transformed into *A. thaliana*. In the *N. benthamiana* leaf epidermal cells, a PKN1-GFP signal was detected in the cytosol, both at the cell membrane and in and around the nucleus, as well as on cortical microtubules (Figure 5I). Microtubule-specific localization was confirmed by the disappearance of the signal following treatment with the microtubule-depolymerizing drug oryzalin (Figure 5J). Confocal imaging of root tips of Arabidopsis plants expressing the *proPKN1:PKN1-GFP* or *pro35S:GFP-PKN1* construct revealed that PKN1 showed a cell cycle phase-dependent intracellular localization pattern (Figure 5, K–P, Supplemental Figure 7, Supplemental Movie 1). In cells going through interphase, the GFP signal was confined to the cytosol, with seemingly a slight enrichment at the nuclear periphery (Figure 5K, Supplemental Figure 7A). Subsequently, before mitosis, a stronger GFP signal was seen at the position of the preprophase band (Figure 5L), while during mitosis, GFP localized at the spindle and the expanding phragmoplast (Figure 5, M–O, Supplemental Figure 7, B and C). Following division, the GFP signal strongly diminished, indicating that PKN1 might be actively broken down after completion of mitosis (Figure 5P, Supplemental Figure 7D). Colocalization experiments with the microtubule-bundling MAP65-1-RFP protein that is known to locate at the preprophase band and the midzone of the anaphase spindle and phragmoplast (Smertenko et al., 2008; Boruc et al., 2017) confirmed PKN1-GFP presence at the different structures enriched in microtubules (Figure 6).

APC/$C^{CCS52A2}$ targets PKN1 for destruction

To investigate whether PKN1 might be targeted for proteasomal destruction, the *proPKN1:PKN1-GUS* reporter line was treated with the proteasome blocker MG-132. To assure that a difference in staining intensity could be observed, GUS staining was purposefully kept short. Under control conditions, no staining could be observed in a weak *proPKN1:PKN1-GUS* line (Figure 7A), while after an overnight treatment with MG-132, the GUS signal was visible throughout the root meristem (Figure 7B). Similarly, a stronger *proPKN1:PKN1-GUS* line showed less signal under control conditions than following MG-132 treatment (Figure 7, C and D). To rule out that the observed effect was due to differences on the transcriptional level, the translational reporter *pro35S:GFP-PKN1* was also tested. As with the GUS reporter, only a faint GFP signal could be observed under control conditions (Figure 7E), whereas following MG-132 treatment, the GFP signal was intense and clearly visible (Figure 7F).

To further test whether PKN1 is marked for breakdown by CCS52A2-mediated APC/C activity, the *proPKN1:PKN1-GUS* reporter line was introgressed into the *ccs52a2-1* mutant background. Interestingly, the root growth of plants homozygous for *ccs52a2-1* and containing the *PKN1-GUS* construct was dramatically reduced compared with *ccs52a2-1* plants without the construct and was often completely stalled (Figure 8, A–E). This phenotype was probably caused by increased PKN1 protein levels, introduced by the reporter construct, again highlighting the need for controlling PKN1 protein abundance through breakdown via CCS52A2. When comparing the PKN1-GUS activity in wild-type versus *ccs52a2-1* plants, the staining in the root meristem appeared more intense in the *ccs52a2-1* background compared with the wild-type background (Figure 8, F–G and I–J), suggesting that PKN1 is indeed targeted for destruction by APC/$C^{CCS52A2}$. Furthermore, meristem organization appeared even more disturbed compared with *ccs52a2-1*, and sporadically meristems were forked (Figure 8H) or completely consumed (Figure 8K). Taken together, these data indicate that it is essential for root meristem development that PKN1 protein abundance is controlled through destruction by APC/$C^{CCS52A2}$.

The PKN1 role in cell division appears conserved in *M. polymorpha*

The *M. Polymorpha* genome holds one putative *PKN1* homologous gene (*Mp7g06500*, Supplemental Dataset 1), nominated *MpPKN1*. As observed for its Arabidopsis counterpart, *MpPKN1* expression was associated with cell division activity, as transcript levels were low in the non-dividing gemmae but strongly increased in 3-day-old dividing young gemmalings (Figure 9A). To confirm its role during cell division, three independent CRISPR/Cas9-based knock-out lines were generated (Figure 9B). One line (#28) holds a single base pair insertion at the first target site (after base pair G^{80}), whereas the other two lines (#5 and #29) hold an inversion of different lengths of the sequence between the two target sites (in between base pairs G^{81} and C^{360}). Wild-type and mutant non-dividing gemmae were indistinguishable, showing an identical epidermal cell number, epidermal cell size, and total plant size (day 0 in Figure 9, C–E). However, three days after cell cycle activation, the mutant gemmalings showed a reduced epidermal cell number compared with wild-type gemmalings (Figure 9C), suggesting an inhibition of cell cycle activity. This was accompanied by a compensatory increase in cell size, most outspoken at the apical notches (Figure 9, D, F and G), leading to the total size of the mutant gemmalings remaining identical to that of the control (Figure 9E). Likewise, the area of 28-day-old mature thalli did not differ between the different genotypes (Figure 9, H–L).

To investigate if the microtubule localization pattern of PKN1 is conserved in Marchantia, a C-terminal GFP translational reporter construct, *pro35S:MpPKN1-GFP*, was transiently transformed into *N. benthamiana* leaves through agroinfiltration, while a C-terminal TdTomato translational reporter construct, *pro35S:MpPKN1-TdTomato*, was stably transformed into Marchantia. For both constructs, imaging

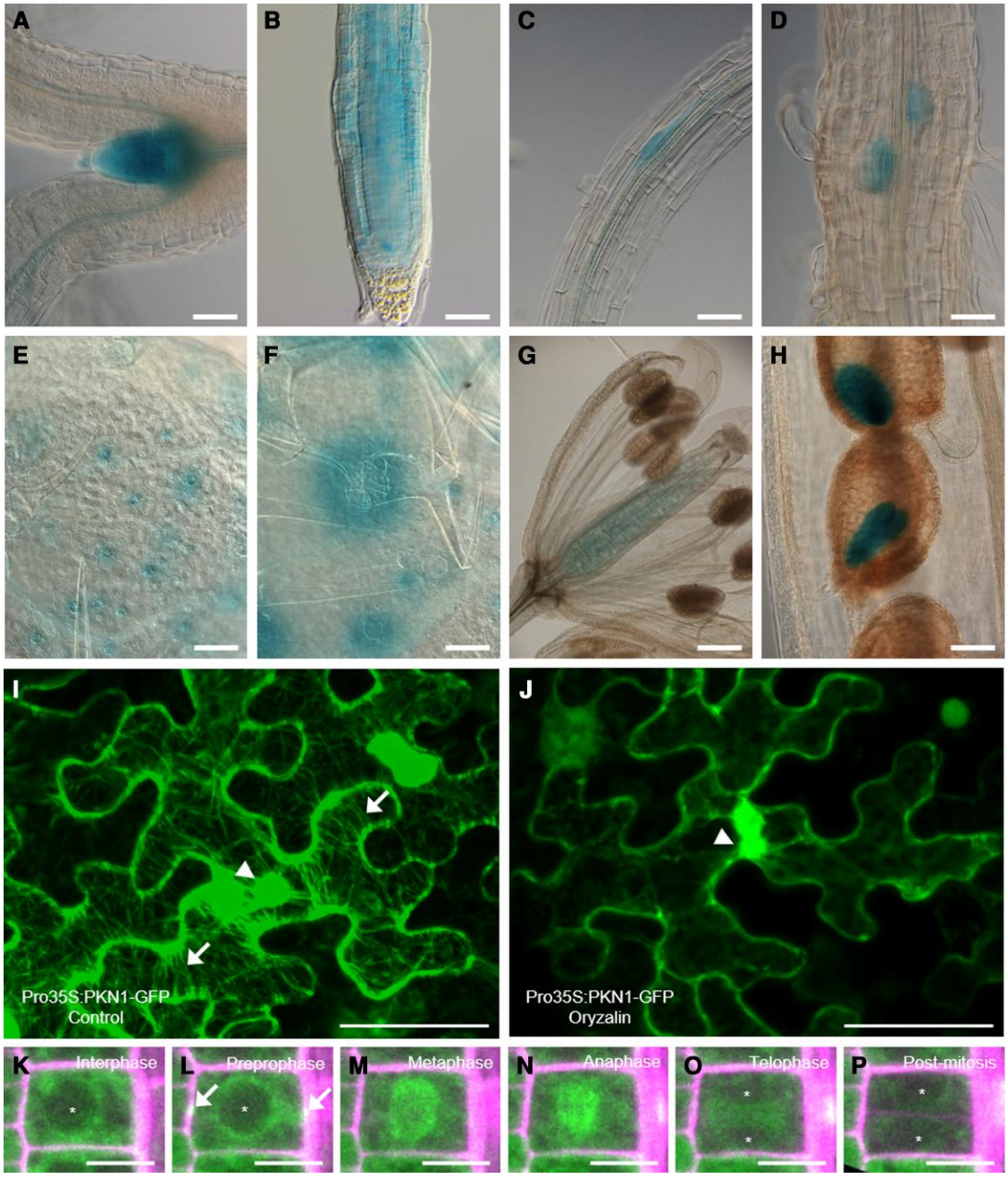

Figure 5 Tissue-specific expression pattern and intracellular localization of PKN1. A–H, Expression of the *proPKN1:PKN1-GUS* construct was detected in the shoot apical meristem and developing young leaves (A), the root apical meristem (B), the adventitious (C) and lateral root initiation sites (D), the stomata (E), the trichome socket cells (F), the developing ovules (G) and the growing embryo (H). Scale bars represent 50 μm (A–F), 500 μm (G) or 100 μm (H). I and J, Transient expression of *pro35S:PKN-GFP* in *N. benthamiana* leaf epidermal cells after agroinfiltration, under control conditions (I) or after a 1.5-h treatment with oryzalin (J). In the control conditions (I), the GFP signal can be seen in the cytosol at the cell membrane, at the nucleus (arrowhead) and on strands of microtubules enveloping the cell (arrows), whereas after treatment with the microtubule-destabilizing drug (J) the microtubule GFP localization signal disappears. Pictures are 3D projections of a Z-stack. Scale bars represent 50 μm. K–P, Expression of *proPKN1:PKN1-GFP* during the cell cycle in a single root meristem cell. The PKN1-GFP protein shows a cell cycle-dependent localization: during interphase (K) it is present in the cytosol but excluded from the nucleus (asterisk); during preprophase (L) it also locates to the preprophase band (arrows); during mitosis (M–O) it appears to locate at the spindle microtubules (M and N) and the phragmoplast (O, asterisks show the newly forming nuclei); post-mitosis its signal is drastically reduced (*P*, asterisks show the newly formed nuclei). Cell walls are visualized through propidium iodide staining. Scale bars represent 10 μm.

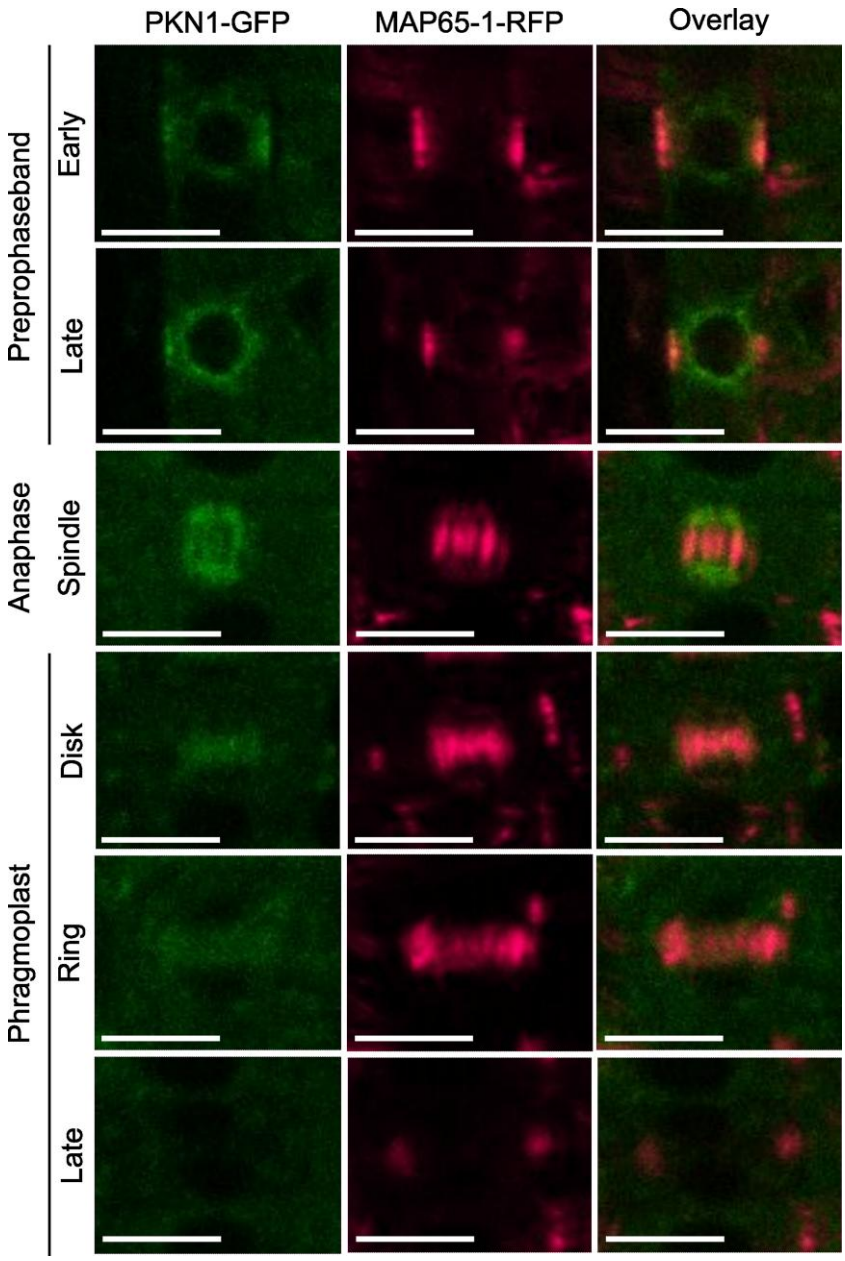

Figure 6 PKN1-GFP localizes at microtubular structures. Visualization of the PKN1 and MAP65-1 proteins in the root tip meristem cells of plants expressing the *proPKN1:PKN1-GFP* and *proAUR1-MAP65-1-RFP* constructs. GFP and RFP signals are shown in green and magenta, respectively. Scale bar represents 10 μm.

revealed fluorescent reporter signals localizing at the cortical microtubules, which could be disrupted through treatment with the microtubule-depolymerizing drug oryzalin (Supplemental Figure 8).

Discussion

PKN1 as a potential target of APC/C^{CCS52A2}

Despite failure to provide direct biochemical proof, our data support the hypothesis that PKN1 might be a direct target of APC/C^{CCS52A2}. First, there is the fact that *pkn1* knock-out mutations can partially recover the *ccs52a2-1* dwarf growth phenotypes, while *ccs52a2-1* mutant plants with a *PKN1* complementation or translational reporter construct show even more severe growth phenotypes, with roots even shorter and sporadically presenting doubled meristems or split root tips, indicating that PKN1 abundance needs to be tightly regulated. Second, the PKN1 amino acid sequence contains several degrons, forming putative recognition sites for APC/C^{CCS52A2}, with their presence being conserved in the identified potential PKN1 homologs throughout the plant kingdom. Third, PKN1 protein levels are increased upon

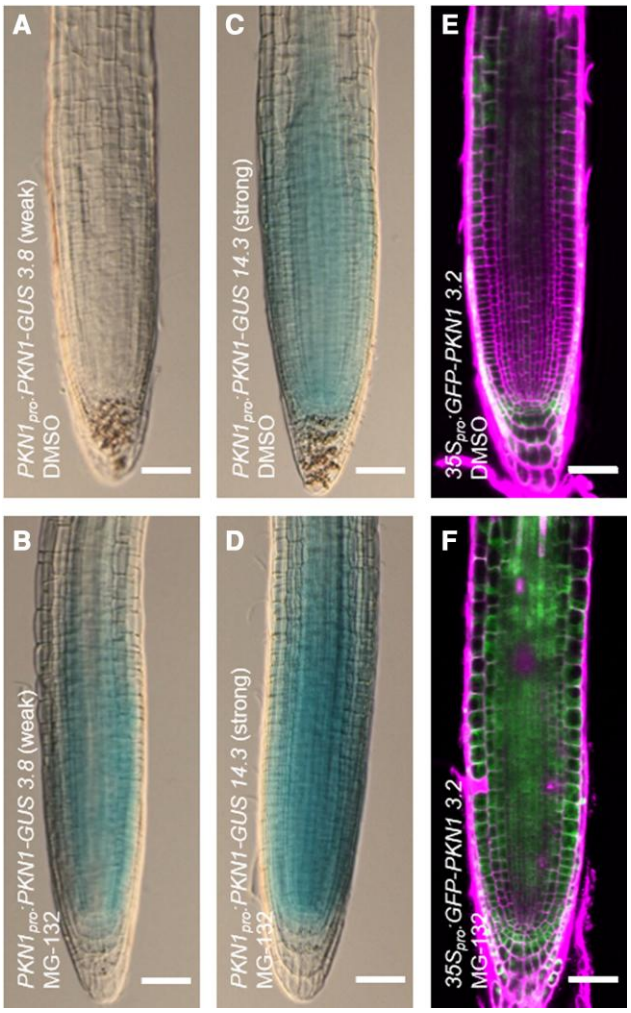

Figure 7 PKN1 is targeted by the 26S proteasome. A–D, Seedlings at 5 DAS of a weak (A and B) and a strong (C and D) *proPKN1:PKN1-GUS* line were treated overnight with DMSO control (A and C) or 100 μM MG-132 dissolved in DMSO (B and D), and subsequently briefly stained with X-Gluc for 60 min at 37°C. Scale bars represent 50 μm. E and F, Seedlings at 5 DAS of a *pro35S:GFP-PKN1* line were treated overnight with DMSO control (E) or 100 μM MG-132 dissolved in DMSO (F), and subsequently imaged through confocal microscopy using identical settings. Cell walls are visualized through propidium iodide staining. Scale bars represent 50 μm.

treatment with a proteasome blocker, making it a likely target of ubiquitination-mediated proteasomal degradation. Finally, time-lapse imaging of PKN1-GFP localization during cell cycle progression revealed a strong decrease in PKN1-GFP levels immediately following cell division, being the moment of highest APC/$C^{CCS52A2}$ activity. All this indicates that CCS52A2-activated APC is marking PKN1 for breakdown to ensure swift progression out of mitosis and thus efficient plant growth. However, attempts to prove direct interaction between PKN1 and CCS52A2 or other APC/C subunits remained fruitless, whereas the severe growth phenotype of the *ccs52a1-1* plants made it impossible to compare relative quantities of cellular PKN1-GFP signals in the wild-type versus mutant meristems, leaving the evidence for the control of CCS52A2 over PKN1 levels to be indirect.

The potential role of PKN1 in the cell cycle

Several lines of evidence point towards PKN1 being a novel plant lineage-specific protein with a role during cell cycle progression. Not only was its expression associated with cell division in both Arabidopsis and Marchantia, but we also demonstrated that the Arabidopsis PKN1 protein displays a cell cycle-dependent subcellular localization. Furthermore, Arabidopsis plants lacking functional PKN1 display a mild reduction in root meristem cell number, while those systemically overexpressing *PKN1* show a small increase in leaf cell number. Likewise, knock-out of the Marchantia *PKN1* gene results in a mild reduction in cell number. For Arabidopsis, it is curious that knock-out and overexpression of *PKN1* seem to specifically affect the root and the leaf, respectively, especially because the gene is expressed in both the root meristem and the developing leaf. One explanation might be that leaf cell number was analyzed at a timepoint where the leaf is thought to be mature (De Veylder et al., 2001; Kheibarshekan Asl et al., 2011). Loss of PKN1 likely only slows down the cell cycle but does not block it, possibly leading only to a delay in leaf development, while still reaching the same end-point cell number as the wild type. In contrast to the leaf, the root meristem is constantly dividing to support continuous root growth, making a delay in cell division more readily visible as a decrease in the pool of meristematic cells present. The fact that plants overexpressing *PKN1* do not show any specific root phenotype might be explained by the fact that the *CaMV 35S* promoter used here can be less active in the root meristem than in other tissues (Ambrose et al., 2011), which was confirmed by the lower level of excess *PKN1* transcripts observed in the root compared with the leaf in these plants.

Arabidopsis PKN1 was observed to display a dynamic localization pattern during the cell cycle, being present at the preprophase band, the spindle and the phragmoplast during preprophase, mitosis, and cytokinesis, respectively. Its potential to associate with microtubules was confirmed by MAP65-1 colocalization experiments, as well as by *N. benthamiana* leaf infiltration experiments showing that PKN1-GFP localization depends on the presence of intact microtubules. Additionally, indirect evidence for a role in determining microtubule dynamics can be found among the set of *PKN1* co-expressed genes, including the microtubule-bundling proteins MICROTUBULE-ASSOCIATED PROTEIN 65-2/3 (MAP65-2/3), the phragmoplast-guiding kinesins PHRAGMOPLAST ORIENTING KINESIN 1/2 (POK1/2), and the microtubule-nucleating and mitotic spindle assembly protein TARGETING PROTEIN FOR XKLP2 (TPX2). Strikingly, our cellular analysis of *ccs52a2-1* indicates that the severe root meristem phenotype of the young seedling is not due to a change in cell division rate, but might rather results from incorrect cell plate positioning, whereas the suppression of this phenotype in the *pkn1-1 ccs52a2-1* double

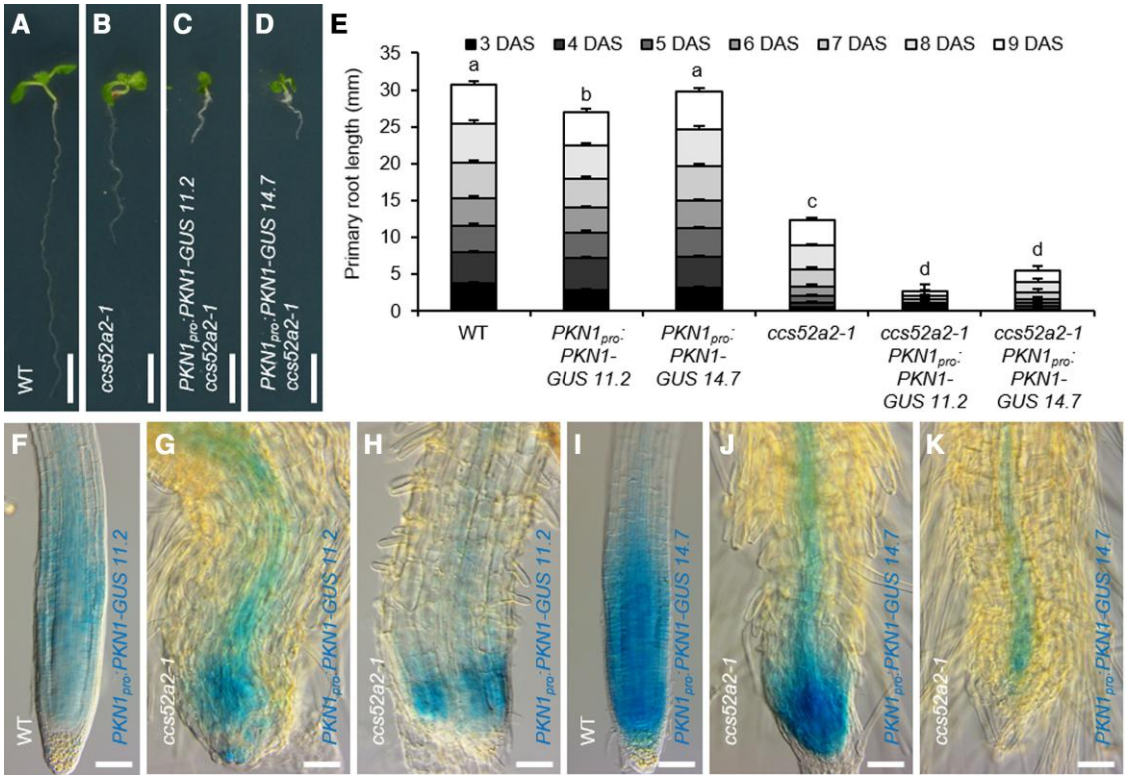

Figure 8 The *proPKN1:PKN1-GUS* reporter in the *ccs52a2-1* background. A–D, Representative seedlings at 9 DAS of the wild type (WT) (A), *ccs52a2-1* (B) and *proPKN1:PKN1-GUS* line 11.2 (C) or line 14.7 (D) in the *ccs52a2-1* background. Scale bars represent 5 mm. E, Primary root length of the respective *proPKN1:PKN1-GUS* lines in the WT and *ccs52a2-1* background from 3 to 9 DAS. Bars represent estimated marginal means and bar heights were subdivided according to the measured daily growth. Error bars represent standard error ($n \geq 13$), and letters indicate statistically different means for each genotype, as calculated for the total root length at 9 DAS ($P < 0.05$, ANOVA mixed model analysis, Tukey correction for multiple testing). F–K, Histochemical GUS staining at 5 DAS of WT (F and I) and *ccs52a2-1* KO (G, H, J and K) root tips with either *proPKN1:PKN1-GUS* 11.2 (F–H), or *proPKN1:PKN1-GUS* 14.7 (I–K) constructs in their background. Roots were stained for 1 h. Scale bars represent 50 µm.

mutant demonstrates dependency on PKN1 activity. Localization of the PKN1-GFP protein at the preprophase band and phragmoplast supports a potential role for PKN1 in establishing correct division plane positioning. However, the absence of a clear cell plate phenotype in the *PKN1*-overexpressing lines indicates that PKN1 likely only participates in this process in coordination with other APC/$C^{CCS52A2}$ targets, thereby only manifesting itself upon mutation of *CCS52A2*.

Following cytokinesis, the *proPKN1:PKN1-GFP* reporter signal disappeared, which would fit the timing of APC/$C^{CCS52A2}$ activation. A similar temporal degradation pattern in a CCS52A2-dependent manner was observed for the cell wall biosynthesis enzyme CSLD5, being important for cellulose deposition at the growing cell wall during cell division (Gu et al., 2016).

PKN1 and *CYCA3;4*

Previously, the causal mutation for *pkn2 ccs52a2-1*, another revertant from the same EMS mutagenesis screen, was shown to be located in the gene coding for the cyclin CYCA3;4 (Willems et al., 2020). The expression profiles of *PKN1* and *CYCA3;4* are markedly similar (Bulankova et al., 2013; Willems et al., 2020) and both genes appear to be co-expressed (Supplemental Figure 9). Moreover, the PKN1 amino acid sequence holds several conserved potential CDK phosphorylation sites, making it a possible phosphorylation target of a CDK activated by CYCA3;4. However, we failed to prove a biochemical interaction between PKN1 and CYCA3;4. Moreover, the respective phenotypes of *PKN1* and *CYCA3;4* knock-out and overexpressing plants are different (Willems et al., 2020). Whereas *pkn1* mutant plants show a reduced root meristem cell division, plants lacking CYCA3;4 seem to have no growth phenotypes. Similarly, *PKN1-* and *CYCA3;4*-overexpressing plants show an increase and decrease in leaf cell number, respectively. Additionally, recovery of the *ccs52a2-1* growth phenotypes in the *pkn1 ccs52a2-1* and *pkn2 ccs52a2-1* double mutants is not the same (Willems et al., 2020). Root growth in the days immediately after germination (3–5 DAS) is substantially better in the *pkn1 ccs52a2-1* mutants than in *pkn2 ccs52a2-1*, accompanied by a more outspoken improvement in root tip tissue organization at 5 DAS. The opposite is seen later during development (6-9 DAS), with *pkn2 ccs52a2-1* showing

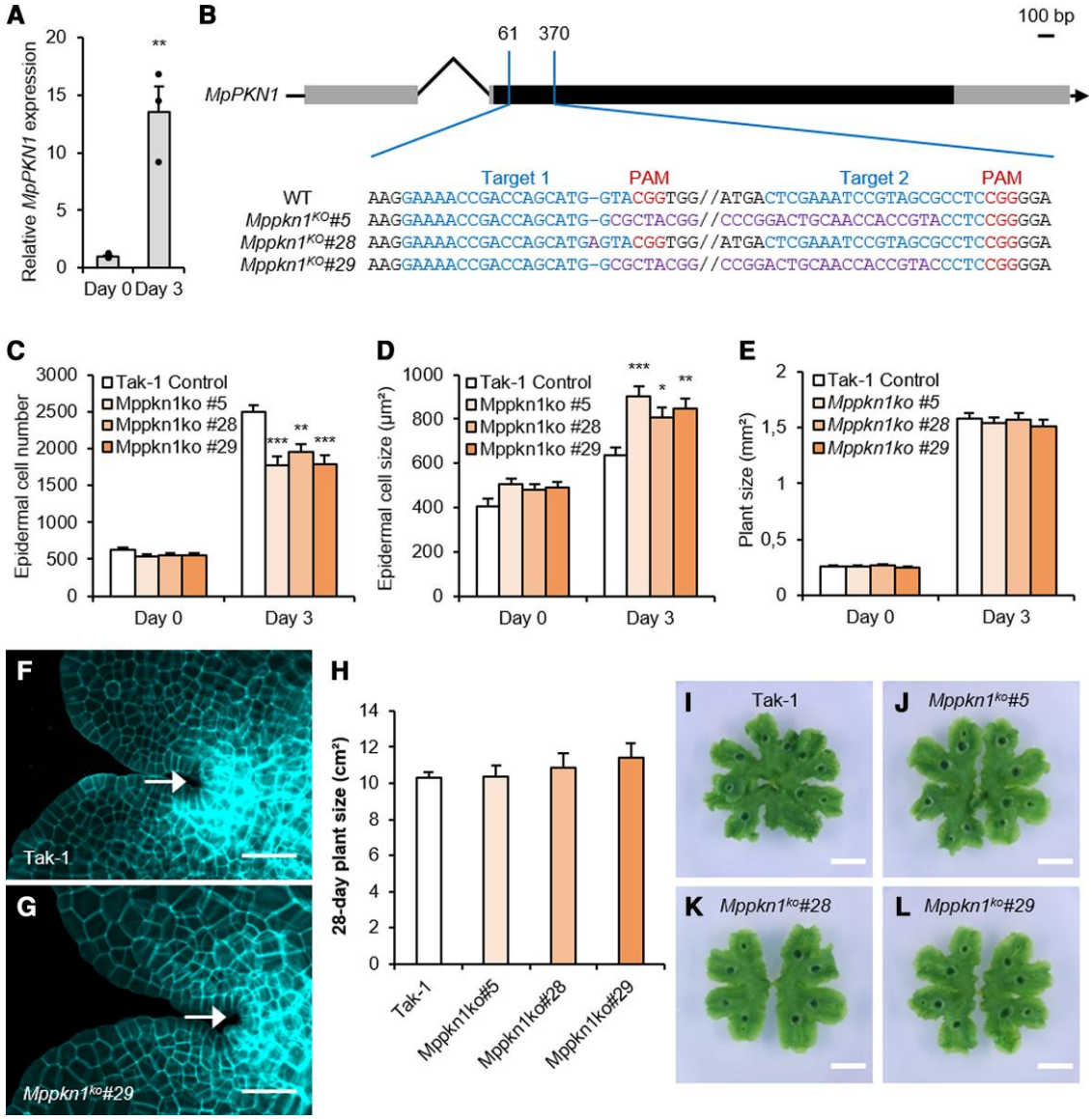

Figure 9 MpPKN1 controls cell division in *Marchantia polymorpha*. A, Time-course of *MpPKN1* expression levels in Tak-1 gemmae (day 0) and 3-day-old gemmalings. Dots represent individual data points ($n = 3$). Error bars represent standard error and asterisks represent means significantly different from the wild-type (WT) mean (T-test with Bonferroni correction for multiple testing, ** $P < 0.01$). B, Gene structure of the *MpPKN1* gene (Mp7g06500, Mapoly0057s0017), showing the three independent CRISPR mutations lines (*#5*, *#28* and *#29*). The gray and black boxes represent the untranslated regions and the coding sequences, respectively, whereas the black line indicates an intron. The blue, red and purple sequences represent the gRNA, PAM site and inverted sequence, respectively. C–E, Epidermal cell number (C), epidermal cell size (D), and plant size (E) of gemmae (day 0) and 3-day-old gemmalings of Tak-1 and *Mppkn1^{ko}#5*, *#28* and *#29*. Error bars represent standard error ($n \geq 6$) and asterisks represent means significantly different from the WT mean (ANOVA with Dunnett correction for multiple testing, * $P < 0.05$, ** $P < 0.01$, *** $P < 0.001$). F and G, Representative images of apical notches of 3-day-old Tak-1 (F) and *Mppkn1^{ko}#29* (G) gemmalings. Cell walls were stained with calcofluor white. The arrows indicate apical notches. Scale bars represent 50 µm. H, Plant size of 28-day-old Tak-1 and *Mppkn1^{ko}#5*, *#28* and *#29* thalli. Error bars represent standard error ($n \geq 6$), no significant difference was found (ANOVA with Dunnett correction for multiple testing at $P < 0.05$). I–L, Aerial view of representative 28-day-old mature Tak-1 and *Mppkn1^{ko}* plants. Scale bars represent 1 cm.

an almost full root meristem cell number recovery in contrast to the *pkn1 ccs52a2-1* mutants whose cell number is not markedly improved compared with *ccs52a2-1*. Moreover, although leaf phenotype recovery in the two revertants is similar and mostly due to an increased cell number, cell size recovery is markedly better in the CRISPR *pkn1 ccs52a2-1* double mutants than in *pkn2 ccs52a2-1*. Taken together, it seems most likely that PKN1 and CYCA3;4 perform independent functions controlling different aspects of meristematic cell division, while being similarly controlled at the protein level by APC/C^{CCS52A2}-mediated breakdown.

In conclusion, PKN1 appears to be a novel and conserved land plant-specific protein playing a role in cell division, likely through its interaction with microtubules, and potentially

being proteolytically controlled by APC/$C^{CCS52A2}$. To determine its exact role during mitosis and its influence on intracellular dynamics, future research might focus on identifying PKN1-interacting proteins, which will also enable the elucidation of the function of its different conserved amino acid regions and shed light on its protein structure.

Materials and methods

Plant medium and growth conditions

Arabidopsis (*A. thaliana*) seeds were sterilized in 70% (v/v) ethanol for 10–15 min and subsequently washed with 100% ethanol, after which they were left to dry in sterile conditions. For all experiments, the seeds were stratified in the dark for 2 days at 4°C before being placed in the growth room. Plants were grown in vitro under long-day conditions (16-h light/8-h dark, Lumilux Cool White lm, 50–70 µmol m^{-2} s^{-1}) at 21°C on solidified half-strength Murashige and Skoog (MS) medium (2.151 g L^{-1}, 10 g L^{-1} sucrose, and 0.5 g L^{-1} 2-(N-morpholino) ethanesulfonic acid (MES), adjusted to pH 5.7 with 1 M KOH and 8 or 10 g L^{-1} plant agar). For analysis of root or shoot phenotypes, plants were grown vertically or horizontally, respectively. The treatments with MG132 were performed at a concentration of 100 µM for 24 h.

M. polymorpha accession Takaragaike-1 (Tak-1) plants were grown under continuous light conditions at 21°C on solidified half-strength Gamborg's B5 medium (Duchefa Biochemie) with 10 g L^{-1} plant agar.

Constructs and lines

The *ccs52a2-1* mutant line has been described previously (Vanstraelen et al., 2009), whereas the *pkn1-1 ccs52a2-1* double mutant was obtained through EMS mutagenesis of *ccs52a2-1* mutant seeds (see below). The *pkn1-1* single mutant was obtained from a segregating population resulting from backcrossing *pkn1-1 ccs52a2-1* with wild-type Col-0 followed by selfing and genotyping. The *pkn1-3* to *pkn1-6* lines were obtained via CRISPR-based targeted mutagenesis in the Col-0 background (see dedicated paragraph).

The *proWOX5:GFP-GUS* transcriptional reporter was previously described (Heyman et al., 2016). The *PKN1* complementation construct *pFAST-R01-PKN1* was created by cloning a fragment containing the *PKN1* promoter (1,500 bp directly upstream from start codon), gene sequence and 3′ untranslated region (300 bp directly downstream from stop codon) from Col-0 into the pDONR221 vector (Invitrogen) via a BP reaction and recombining it into the pFAST-R01 vector (Shimada et al., 2010) via an LR reaction. The $PKN1^{OE}$ construct was created by cloning the *PKN1* open reading frame (ORF) including stop codon from Col-0 into pDONR221 (Invitrogen, creating pDONR221-PKN1) via a BP reaction and subsequently recombining it via an LR reaction behind the strong *CaMV* 35S promoter in the pB7WG2 vector (Karimi et al., 2002). To create the PKN1 translational reporter lines, a PKN1 promoter fragment (consisting of 1,500 bp upstream of the start codon) was cloned via a BP reaction into the pDONR-P4-P1r entry vector (Invitrogen, creating pDONR-L4-proPKN1-R1) and the *PKN1* ORF without stop codon was cloned via a BP reaction into pDONR221 (Invitrogen, creating pDONR221-PKN1nostop). The *pro35S:PKN1-GFP* construct was created by recombining pDONR221-PKN1nostop via an LR reaction behind the *CaMV 35S* promoter and in front of GFP in the pK7FWG2 vector (Karimi et al., 2002). The *pro35S:GFP-PKN1* construct was created by recombining pDONR221-PKN1 via an LR reaction behind the *CaMV 35S* promoter and GFP in the pK7WGF2 vector (Karimi et al., 2002). The *proPKN1:PKN1-GFP* and *proPKN1:PKN1-GUS* translational reporter constructs were created by recombining pDONR-L4-proPKN1-R1, pDONR221-PKN1nostop and pEN-R2-F*-L3 (GFP) or pEN-R2-S*-L3 (GUS) via an LR reaction into the pK7m34GW destination vector (Karimi et al., 2005, 2007). The proAUR1:MAP65-1-RFP translational reporter line was previously described (Boruc et al., 2017). All primer sequences used for cloning and genotyping are listed in Supplemental Table 4.

All vector-based cloning for Arabidopsis constructs was performed using the Gateway system (Invitrogen) according to the manufacturer's recommendations. All constructs were transferred into the *Agrobacterium tumefaciens* C58C1RifR strain harboring the pMP90 plasmid. The obtained Agrobacterium strains were used to generate stably transformed Arabidopsis lines with the floral dip transformation method (Clough and Bent, 1998). All constructs were transformed into the Col-0 background, except for the *PKN1* complementation construct, which was transformed into *pkn1-1 ccs52a2-1*. Successful transformants were selected using kanamycin or Basta (glufosinate ammonium) or using fluorescence microscopy in the case of FAST constructs. In the T2 generation, only lines containing a single insert location of the construct were retained, while homozygous lines were selected in the T3 generation. Double mutants were made by crossing and confirmed through genotyping with PCR and/or sequencing.

For Marchantia constructs, the Tak-1 *MpPKN1* (Mapoly 0057s0017, Mp7g06500) ORF without stop codon was cloned into pDONR221 (Invitrogen, creating pDONR221-MpPKN1 nostop) via a BP reaction. The *pro35S:MpPKN1-GFP* construct was created by recombining pDONR221-MpPKN1nostop via an LR reaction behind the *CaMV 35S* promoter and in front of GFP in the pH7m34GW vector (Karimi et al., 2002). The *pro35S:MpPKN1-Tdtomato* construct was created by recombining pDONR221-MpPKN1nostop via an LR reaction into the pMpGWB130 vector (Ishizaki et al., 2015). Agrobacterium-mediated *M. polymorpha* Tak-1 transformation was done as previously described (Kubota et al., 2013). Transformants were selected on medium containing 10 mg L^{-1} hygromycin and 100 µg mL^{-1} cefotaxime.

Generating CRISPR mutants

To generate the *A. thaliana PKN1* CRISPR mutants, two gRNAs specific for *PKN1* (gRNA1, TCAGTCTCAGCCAC AGCCGC; gRNA3, ACTGATCTCACTGGTCTACG) were

selected using the CRISPR-P web tool based on the expected cut site in the beginning of the gene (behind base pair 64 and 286 of the *PKN1*-coding sequence, respectively) and minimal off-target scores (Lei et al., 2014). Primer pairs for the two gRNAs were designed to include 5′-end overhangs, being ATTG for the forward primer and AAAC for the reverse complement primer. The gRNA1 and gRNA3 primer pairs were inserted into the pGG-A-ATU6PTA-B and pGG-B-ATU6PTA-C vectors, respectively, after which these were recombined with the pGG-C-LinkerII-G vector into the pEN-L1-AG-L2 acceptor plasmid using Golden Gate, as previously described (Houbaert et al., 2018). This gRNA Gateway entry clone was then recombined with the pEN-L4-RPS5P-Cas9PTA-G7T-R1 and pB7m24GW3-FAST destination vectors in a Multisite Gateway LR reaction according to the manufacturer's recommendations (Karimi et al., 2007; Houbaert et al., 2018). The construct was transformed into Col-0 plants as described in the previous paragraph, and successful transformants were selected using fluorescence microscopy on T1 generation seeds. T2 generation plants without the CRISPR construct were obtained by looking for seeds without fluorescence obtained from different T1 generation plants. Plants mutated at the expected sites were identified through SNP-genotyping PCR and sequencing, as previously described (Houbaert et al., 2018). All primer sequences used are listed in Supplemental Table 4.

To generate the *M. polymorpha PKN1* CRISPR mutants, the established CRISPR/Cas9-mediated mutagenesis system in *Marchantia* was used to generate *MpPKN1* mutant lines (Sauret-Güeto et al., 2020). Two different single gRNAs specific for *MpPKN1* (gRNA1: 5′-GAAAACCGACCAGCATGGTA-3′ and gRNA2: 5′-CTCGAAATCCGTAGCGCCTC-3′) were selected using the CRISPR direct web tool (https://crispr.dbcls.jp/) based on the expected cut site in the beginning of the gene (behind base pair 63 and 344 of the *PKN1*-coding sequence, respectively) and minimal off-target scores. The gRNA1 and gRNA2 primer pairs were inserted into the L1_lacZgRNA-Ck2 (OP-075) and L1_lacZgRNA-Ck3 (OP-074) vectors, respectively, after which these were recombined with the L1_CsR-Ck1(OP-062) and L1_Cas9-Ck4 (OP-073) vector into the pCsA (OP-005) acceptor plasmid using Golden Gate Loop Assembly according to the manufacturer's recommendations (Sauret-Güeto et al., 2020). The construct was transformed into Tak-1 background plants and transformants were selected with 0.5 μM chlorsulfuron (Sigma–Aldrich) and 100 μg mL^{-1} cefotaxime, fully frame-shifted transgenic lines were selected for further experiments. To genotype the mutant lines carrying a large deletion or inversion, the following primer sequences were used: 5′-TCACAACATACGTCCGACTAC −3′ and 5′-TCGGAGTGACGAGGGATGAA-3′.

Plant growth phenotyping

Root growth and length were determined by marking the position of the root tip each day from 3 to 9 DAS, scanning the plates at 9 DAS and measuring using the ImageJ software package. Root meristem analysis was performed with the ImageJ software package using images of the root tip, the distance between the QC and the end of the division zone was measured to determine the root meristem length, the number of cortical cells within the division zone was counted to determine the cortical cell number, and the average cortical cell size was determined by dividing the measured meristem length by the number of cortical cells.

To determine the rosette size, pictures were taken at 21 DAS using a digital camera fixed in position, after which the images were made binary (black and white) and the projected rosette size was measured using the wand tool in ImageJ. For analysis of leaf parameters, the first leaf pairs were harvested at 21 DAS and cleared overnight using 100% ethanol. Next, leaves were mounted on a slide with lactic acid. The total leaf area was determined from images taken with a digital camera mounted on a Stemi SV11 microscope (Zeiss) using ImageJ software. A DM LB microscope (Leica) with a drawing-tube attached was used to generate a pencil drawing of a group of at least 30 cells of the abaxial epidermis. On each leaf, the area chosen for drawing was located between 25% and 75% of the distance between the tip and the base of the leaf, halfway between the midrib and the leaf margin. After measuring the total drawn area (using the wand tool of ImageJ) and counting the number of pavement cells and stomata drawn, the average cell size, total number of cells per leaf, and the SI (the number of stomata divided by the total number of epidermal cells) were calculated.

For *Marchantia* gemma and gemmaling size, the obtained confocal images were made binary (black and white) and the plant size was measured using the wand tool in ImageJ. For *Marchantia* gemma and gemmaling epidermal cell number, the obtained confocal images were analyzed in ImageJ running a macro script from The BioVoxxel Image Processing and Analysis Toolbox as previously described (Li et al., 2020). Epidermal cell density was calculated by dividing the plant size by the epidermal cell number.

Flow cytometry

For flow cytometry analysis, leaf material was chopped in 200 μL nuclei extraction buffer, after which 800 μL staining buffer was added (Cystain UV Precise P, Partec). The mix was filtered through a 30-μm green CellTrics filter (Sysmex – Partec) and analyzed by the Cyflow MB flow cytometer (Partec). The Cyflogic software was used for ploidy measurements. To calculate the EI, the following formula was used, with %*n*C representing the fraction of nuclei with n-times the haploid genome content:

$$\frac{0 \times \%2C + 1 \times \%4C + 2 \times \%8C + 3 \times \%16X + 4 \times \%32C}{\text{Total nuclei}}$$

Confocal microscopy

For visualization of Arabidopsis root apical meristems, vertically grown plants were mounted in a 10-μM propidium

iodide (PI) solution (Sigma) to stain the cell walls. Images were obtained with confocal microscopy using an LSM 5 Exciter (Zeiss) confocal microscope. For PI and GFP excitation, the 543 line of a HeNe laser and the 488 line of an Argon laser were used, respectively. Laser light passed through an HFT 405/488/543/633 primary dichroic beamsplitter before reaching the sample and emitted light from the sample first passed through an NFT 545 secondary dichroic beamsplitter, after which it passed through a 650-nm longpass filter for PI detection and through a 505- to 530-nm bandpass filter for detection of GFP. PI and GFP were detected simultaneously with the line scanning mode of the microscope. Agroinfiltrated *N. benthamiana* leaf cuttings were mounted in H_2O. Imaging was done using an LSM 5 Exciter (Zeiss) confocal microscope, using identical settings as described above. Staining and visualization of young root stem cells was performed as described (Truernit et al., 2008). For each root, an identical meristem surface area was counted.

For the pPKN1-PKN1-GFP movie and extracted stills used in Figure 5, K–P, imaging was performed using a Zeiss LSM900 confocal microscope. GFP and PI were excited with a 488-nM laser while PI was excited with a 559-nm laser. GFP emission (green) was collected between 500–535 nm whereas PI emission (cyan) was collected between 575–700 nm by GaAsP-PMT detectors at 8-min intervals. The images were registered and processed further via ImageJ for generating still images and movies.

For PKN1-GFP and MAP65-1-RFP colocalization in *A. thaliana* root meristematic cells, 1-week-old seedlings were imaged. Images were acquired using an LSM 710 (Zeiss) confocal microscope, GFP signal was observed using 488 nm excitation and 500–530 nm emission, whereas for RFP, 561 nm excitation and 570–600 nm emission, setting were used.

Marchantia plants were visualized using an LSM 710 (Zeiss) confocal microscope. Gemmae and 1-day-old gemmalings were mounted in a 10-µM PI solution (excitation 488 nm, emission 555–600 nm) as previously described (Westermann et al., 2020), while 2- and 3-day-old gemmalings were vacuum-infiltrated with ClearSee containing 0.1% calcofluor white (excitation 405 nm, emission 415–443 nm) prior to mounting according to the ClearSee protocol (Ursache et al., 2018). The $35S_{pro}$:*MpPKN1-Tdtomato Marchantia* thalli were grown for 14 days in half-strength B5 medium before transfer to either DMSO control or oryzalin (10 µM in DMSO) in half-strength B5 liquid medium for 1 h. To observe fluorescence, excitation at 561 nm and emission at 570–600 nm were used for TdTomato.

EMS mutagenesis

Roughly 14,000 *ccs52a2-1* seeds were subjected to EMS mutagenesis. The seeds were first hydrated with H_2O for 8 h on a rotating wheel before being mutagenized with a 0.25% v/v solution of EMS for another 12 h. After treatment, seeds were washed twice with 15 mL of 0.1 M sodium thiosulfate ($Na_2S_2O_3$) for 15 min to stop the reaction and subsequently twice with H_2O for 30 min. After that, seeds were left to dry on Whatman paper. Fifty-six pools of approximately 250 M_1 seeds were mixed together with fine sand in Eppendorf tubes and sown in big pots with standard soil. After selfing, M_2 seeds were harvested separately for every pool. Seeds were sterilized and sown on vertical plates to score for the reversion of the *ccs52a2-1* root growth phenotype. Plants with longer roots were subsequently selected and transferred to soil for self-fertilization. The recovery phenotype was then reconfirmed in the next generation (M_3).

Mapping of the revertant mutation

Segregating F2 progeny resulting from a cross between *pkn1-1 ccs52a2-1* and the *ccs52a2-1* parental line used for EMS mutagenesis was used as a mapping population. Approximately 250 plants showing the long root phenotype of the revertant were selected at 5 DAS and pooled for DNA extraction using the DNeasy Plant Mini Kit (Qiagen) according to the manufacturer's instructions. DNA was extracted additionally from 200 plants of the original *ccs52a2-1* parental line. Illumina True-Seq libraries were generated from the extracted DNA according to the manufacturer's protocol and sequenced on an Illumina HiSeq 100-bp paired-end run. The SHORE pipeline (Ossowski et al., 2008) was used for the alignment of sequences of both *pkn1-1 ccs52a2-1* and *ccs52a2-1* to the reference genome (Col-0; TAIR10). Using the SHOREmap pipeline (Sun and Schneeberger, 2015), an interval of increased mutant SNP alleles was identified and subsequently annotated. Filtering was performed within the interval for de novo EMS-specific SNPs with a concordance above 0.8 and intergenic or intronic mutations were removed to reveal the potential revertant mutations.

Co-expression analysis of high-concordance loci

To gain functional understanding of the four candidate loci, each candidate's co-expression neighborhood was queried for overrepresented functions, using 18 RNA-seq data sets (Depuydt and Vandepoele, 2021). In short, each data set was processed using Prose (Vaneechoutte and Vandepoele, 2019) to generate 18 expression atlases, from which transcriptome-wide co-expression networks were built. Next, the co-expression neighborhoods of each candidate locus, identified using the vHRR method, were extracted, followed by gene set enrichment analysis to identify overrepresented GO terms in each neighborhood. Enrichment statistics were calculated using Fisher's exact test, followed by a Benjamini-Hochberg multiple testing correction (Benjamini and Hochberg 1995). GO annotations with experimental and curated evidence codes were downloaded from The Arabidopsis Information Resource (version 01/01/2021; (Berardini et al., 2015).

SNP-genotyping PCR

The SNP-genotyping PCRs were performed as described previously (Mesrian Tanha et al., 2015), except that primer pairs specific for the wild-type or mutant allele were not combined

in a single reaction, but rather used in separate PCR reactions in order to increase specificity. Prior to genotyping, test PCRs were performed to establish the most suitable annealing temperature for each used primer pair. All primer sequences used for the SNP-genotyping PCR are listed in Supplemental Table 4.

Identification of homologs and conserved motifs

The dicotyledon PKN1 homolog sequences and that of *A. trichopoda* were obtained from Dicot PLAZA 4.5 (https://bioinformatics.psb.ugent.be/plaza/versions/plaza_v4_5_dicots/, (Van Bel et al., 2018)) under the homologous gene family HOM04D007290, while the monocotyledon homolog sequences were obtained from Monocot PLAZA 4.5 (https://bioinformatics.psb.ugent.be/plaza/versions/plaza_v4_5_monocots/, (Van Bel et al., 2018)) under the homologous gene family HOM04 × 5M006718. The gymnosperm PKN1 homolog sequences were obtained from Gymnosperm PLAZA 1.0 (https://bioinformatics.psb.ugent.be/plaza/versions/gymno-plaza/, (Proost et al., 2015)) under the homologous gene family HOM03D007930, which was identified using PLAZA's internal BlastP functionality with default settings searching for sequences producing significant alignments with the *A. thaliana* PKN1 (alignment scores ranged from 47.8 to 60.5, with E-values ranging from $2e^{-5}$ to $1e^{-9}$). The PKN1 homologs of *M. polymorpha* and *P. patens* were identified using the internal BlastP functionality of Dicot PLAZA 4.5 with default settings, except that the E-value threshold was changed to 0.001, searching for sequences producing significant alignments with the *A. thaliana* PKN1 (alignment scores ranged from 50.4 to 52.8, with E-values ranging from $1e^{-4}$ to $3e^{-5}$). The PKN1 homologs of *S. moellendorffii* were identified using BlastP (https://blast.ncbi.nlm.nih.gov/Blast.cgi?PAGE=Proteins, (Johnson et al., 2008)) with the default settings, searching for sequences producing significant alignments with the *M. polymorpha* PKN1 within the *S. moellendorffii* non-redundant protein sequence database (alignment scores were 54.7, with an E-value of $3e^{-7}$), with sequences obtained from the RefSeq database (https://www.ncbi.nlm.nih.gov/refseq/). All sequences used are listed in Supplemental Dataset 1.

For motif discovery, the MEME (Bailey and Elkan, 1994) and MAST (Bailey and Gribskov, 1998) web-tools, part of the MEME Suite (https://meme-suite.org/meme/), were used. For input in MEME, a FASTA-type sequence file was compiled containing the PKN1 homologs from the different plant species. When species contained multiple putative PKN1 paralogs, only the most conserved (i.e. most similar to *A. thaliana* PKN1) was used. Furthermore, homolog sequences that appeared to have been incorrectly annotated or were otherwise problematic, for example by being very short, split over multiple genes or missing stretches of sequence, were not used. See also Supplemental Dataset 1, column "Used for MEME". MEME was run using the default settings, except that the number of motifs to be found was set at 10. The Supplemental Dataset 1 file contains the resulting MEME and MAST output web pages, available as HTML and as simple text file, as well as the exact sequences of the discovered motifs in the different species, available in FASTA and raw format. Logos of the ten different motifs were designed with the Weblogo3 web tool (weblogo.threeplusone.com/create.cgi), using the raw format motif sequences as input and using the default settings, with the following adjustments: Output Format was set at "PNG (high res)", Sequence Type was set at "Protein", Composition was set at "No adjustment for composition", the Error Bars box was unchecked, the Version Fineprint box was unchecked, Y-axis Tic Spacing was set at "2", and Color Scheme was set at "Chemistry (AA)".

RT-PCR and rt-qPCR

RNA was isolated with the RNeasy Mini kit (Qiagen) and was treated on-column with the RQ1 RNase-Free DNase (Promega) and used for cDNA synthesis with the iScript cDNA Synthesis Kit (Bio-Rad). For RT-PCR on the *pkn1-2* T-DNA line, cDNA made from RNA extracted from *pkn1-2* and Col-0 was used as a template for PCR using *PKN1* primers (see Supplemental Table 2) and the resulting amplicons were separated on a 1% agarose gel containing SYBRSafe (Invitrogen). RT-qPCR was performed using the SYBR Green kit (Roche) with 100 nM primers and 0.125 µl of RT reaction product in a total volume of 5 µl per reaction. Reactions were run and analyzed on the LightCycler 480 (Roche) according to the manufacturer's instructions. For Arabidopsis, *EMB2386*, *PAC1*, and *RPS26E* were used as reference genes for normalization. For *Marchantia*, *MpEF1α* (Mp3g23400, Mapoly0024s0116) and *MpActin* (Mp6g11010, Mapoly0016s0139) were used as reference genes for normalization (Saint-Marcoux et al., 2015). For each reaction, three technical repeats were performed. All primer sequences used for RT-qPCR are listed in Supplemental Table 4.

GUS staining

Plants were grown for the indicated period and fixed in an ice-cold 80% acetone solution for 3 h. Samples were washed three times with phosphate buffer (14 mM NaH_2PO_4 and 36 mM Na_2HPO_4) before being incubated in staining buffer (0.5 mg mL^{-1} 5-bromo-4-chloro-3-indolyl-β-D-glucuronic acid, 0.165 mg mL^{-1} potassium ferricyanide, 0.211 mg mL^{-1} potassium ferrocyanide, 0.585 mg mL^{-1} EDTA pH8, and 0.1% (v/v) Triton-X100, dissolved in phosphate buffer) at 37°C between 30 min and 16 h until sufficient staining was observed.

Agroinfiltration

Wild-type *N. benthamiana* plants were grown under a normal light regime (14 h of light, 10 h of darkness) at 25°C and 70% relative humidity. The constructs were transferred using electroporation into the *A. tumefaciens* strain LBA4404 harboring the virulence plasmid VirG. The transformed Agrobacterium strain harboring the construct of interest was grown for 2 days in a shaking incubator (200 rpm) at 28°C in 10 mL of yeast extract broth medium, supplemented with the appropriate

antibiotics. After incubation, the OD600 of each culture was measured with a spectrophotometer and an amount of culture representing an OD600 of 1.5 in a final volume of 2 mL was transferred to a fresh tube and spinned down. The resulting pellets were resuspended in 2 mL of infiltration buffer (10 mM $MgCl_2$, 10 mM MES at pH 5.6, 100 µM acetosyringone) and 3× diluted with infiltration buffer (representing a final OD600 of 0.5) before infiltration. The inoculum was delivered to 3- to 4-week-old *N. benthamiana* leaves by gentle pressure infiltration of the lower epidermis with a 1-mL syringe without needle. The infiltrated area of the leaf was delimited and labeled with permanent marker. The plant was incubated under normal growing conditions and expression of *GFP* was observed using confocal microscopy 3–5 days after infiltration. For pharmacological analysis, leaves infiltrated with $35S_{pro}$*:MpPKN1-GFP* containing Agrobacterium were infiltrated after three days with DMSO or oryzalin (10 µM in DMSO) for a 1 h treatment, as described previously (Boruc et al., 2019).

Statistical analysis

Statistical analyses were performed as indicated in the figure legends.

Accession numbers

A. thaliana sequence data from this article can be found in the Arabidopsis Genome Initiative or GenBank/EMBL databases under the following accession numbers: *CCS52A2* (AT4G11920), *PKN1* (AT2G43990), *WOX5* (AT3G11260), *EMB2386* (AT1G02780), *PAC1* (AT3G22110), and *RPS26E* (AT3G56340). *M. polymorpha* sequence data can be found in the PLAZA or MarpolBase databases under the following accession numbers: *MpPKN1* (Mapoly0057s0017 or Mp7g06500), Mp*EF1α* (Mapoly0024s0116 or Mp3g23400) and Mp*Actin* (Mapoly0016s0139 or Mp6g11010). The source and accession numbers of the *PKN1* homologs can be found in Supplemental Dataset 1.

Supplemental data

The following supplemental materials are available.

Supplemental Figure S1. Additional characteristics of the *ccs52a2-1* and *pkn1-1 ccs52a2-1* mutants.

Supplemental Figure S2: Root stem cell niche in the *ccs52a2-1*, *pkn1-1* and *pkn1-1 ccs52a2-1* mutants.

Supplemental Figure S3. Cell number quantification in the *ccs52a2-1*, *pkn1-1* and *pkn1-1 ccs52a2-1* mutants.

Supplemental Figure S4. Detail of the allele frequency of EMS-specific mutations in *pkn1-1 ccs52a2-1*.

Supplemental Figure S5. Conserved motifs in the PKN1 protein.

Supplemental Figure S6. *PKN1* expression levels in wild-type and $PKN1^{OE}$ shoots and roots.

Supplemental Figure S7. Intracellular localization of GFP-PKN1.

Supplemental Figure S8. *MpPKN1* subcellular localization.

Supplemental Figure S9. Network of *PKN1* co-expressed genes.

Supplemental Table S1. Detailed annotation of the SNPs found for *pkn1-1 ccs52a2-1* in the interval selected on Chromosome 2 from 17 Mbp up to the end.

Supplemental Table S2. Co-expression-based gene ontology predictions for AT2G43990 using vHRR

Supplemental Table S3. Co-expression neighborhood of AT2G43990 in the ERP109042 network.

Supplemental Table S4. Primer sequences.

Supplemental Dataset S1. *PKN1* homologs.

Supplemental Movie S1. Time-lapse confocal imaging of a PI-stained (Magenta) *pPKN1:PKN1-GFP* seedling 3 days after germination.

Acknowledgments

The authors thank Annick Bleys for help in preparing the manuscript, and Daniel Van Damme and Evelien Mylle for their help with confocal imaging.

Funding

This work was supported by a grant of the Research Foundation Flanders (G0010820N). A.W. is indebted to the Agency for Innovation by Science and Technology in Flanders for a predoctoral Fellowship. J.H. is indebted to the Research Foundation Flanders for a postdoctoral fellowship. Y.L was supported by the China Scholarship Council for a predoctoral scholarship (201806910058).

Conflict of interest statement. The authors have no conflict of interest.

References

Ambrose C, Allard JF, Cytrynbaum EN, Wasteneys GO (2011) A CLASP-modulated cell edge barrier mechanism drives cell-wide cortical microtubule organization in Arabidopsis. Nat Commun **2**: 430

Bailey TL, Elkan C (1994). Fitting a mixture model by expectation maximization to discover motifs in biopolymers. *In* Altman R, Brutlag D, Karp P, Lathrop R, Searls D, eds, Proceedings of the Second International Conference on Intelligent Systems for Molecular Biology. Menlo Park, CA: AAAI Press, pp. 28–36

Bailey TL, Gribskov M (1998) Combining evidence using p-values: application to sequence homology searches. Bioinformatics **14**(1): 48–54

Baloban M, Vanstraelen M, Tarayre S, Reuzeau C, Cultrone A, Mergaert P, Kondorosi E (2013) Complementary and dose-dependent action of AtCCS52A isoforms in endoreduplication and plant size control. New Phytol **198**(4): 1049–1059

Benjamini Y, Hochberg Y (1995) Controlling the false discovery rate: a practical and powerful approach to multiple testing. J. R. Stat. Soc. B **57**(1): 289–300

Berardini TZ, Reiser L, Li D, Mezheritsky Y, Muller R, Strait E, Huala E (2015) The Arabidopsis information resource: making and mining the "gold standard" annotated reference plant genome. Genesis **53**(8): 474–485

Boruc J, Deng X, Mylle E, Besbrugge N, Van Durme M, Demidov D, Dvořák Tomaštíková E, Tan T-RC, Vandorpe M, Eeckhout D, et al.

(2019) TPX2-LIKE PROTEIN3 is the primary activator of α-aurora kinases and is essential for embryogenesis. Plant Physiol **180**(3): 1389–1405

Boruc J, Weimer AK, Stoppin-Mellet V, Mylle E, Kosetsu K, Cedeno C, Jaquinod M, Njo M, De Milde L, Tompa P, et al. (2017) Phosphorylation of MAP65-1 by Arabidopsis Aurora kinases is required for efficient cell cycle progression. Plant Physiol **173**(1): 582–599

Boudolf V, Lammens T, Boruc J, Van Leene J, Van Den Daele H, Maes S, Van Isterdael G, Russinova E, Kondorosi E, Witters E, et al. (2009) CDKB1; 1 forms a functional complex with CYCA2; 3 to suppress endocycle onset. Plant Physiol **150**(3): 1482–1493

Bulankova P, Akimcheva S, Fellner N, Riha K (2013) Identification of *Arabidopsis* meiotic cyclins reveals functional diversification among plant cyclin genes. PLoS Genet **9**(5): e1003508

Clough SJ, Bent AF (1998) Floral dip: a simplified method for *Agrobacterium*-mediated transformation of *Arabidopsis thaliana*. Plant J **16**(6): 735–743

Cromer L, Jolivet S, Horlow C, Chelysheva L, Heyman J, De Jaeger G, Koncz C, De Veylder L, Mercier R (2013) Centromeric cohesion is protected twice at meiosis, by SHUGOSHINs at anaphase I and by PATRONUS at interkinesis. Curr Biol **23**(21): 2090–2099

Cromer L, Jolivet S, Singh DK, Berthier F, De Winne N, De Jaeger G, Komaki S, Prusicki MA, Schnittger A, Guérois R, et al. (2019) Patronus is the elusive plant securin, preventing chromosome separation by antagonizing separase. Proc Natl Acad Sci U S A **116**(32): 16018–16027

da Fonseca PCA, Kong EH, Zhang Z, Schreiber A, Williams MA, Morris EP, Barford D (2011) Structures of APC/C^{Cdh1} with substrates identify Cdh1 and Apc10 as the D-box co-receptor. Nature **470**(7333): 274–278

Depuydt T, Vandepoele K (2021) Multi-omics network-based functional annotation of unknown Arabidopsis genes. Plant J **108**(4): 1193–1212

De Veylder L, Beeckman T, Beemster GTS, Krols L, Terras F, Landrieu I, Van Der Schueren E, Maes S, Naudts M, Inzé D (2001) Functional analysis of cyclin-dependent kinase inhibitors of Arabidopsis. Plant Cell **13**(7): 1653–1668

De Veylder L, Beeckman T, Inzé D (2007) The ins and outs of the plant cell cycle. Nat Rev Mol Cell Biol **8**(8): 655–665

Eloy NB, de Freitas Lima M, Van Damme D, Vanhaeren H, Gonzalez N, De Milde L, Hemerly AS, Beemster GTS, Inzé D, Ferreira PCG (2011) The APC/C *subunit 10* plays an essential role in cell proliferation during leaf development. Plant J **68**(2): 351–363

Eloy NB, Gonzalez N, Van Leene J, Maleux K, Vanhaeren H, De Milde L, Dhondt S, Vercruysse L, Witters E, Mercier R, et al. (2012) SAMBA, a plant-specific anaphase-promoting complex/cyclosome regulator is involved in early development and A-type cyclin stabilization. Proc Natl Acad Sci U S A **109**(34): 13853–13858

Eme L, Trilles A, Moreira D, Brochier-Armanet C (2011) The phylogenomic analysis of the anaphase promoting complex and its targets points to complex and modern-like control of the cell cycle in the last common ancestor of eukaryotes. BMC Evol Biol **11**: 265

Fülöp K, Tarayre S, Kelemen Z, Horváth G, Kevei Z, Nikovics K, Bakó L, Brown S, Kondorosi A, Kondorosi E, et al. (2005) Arabidopsis anaphase-promoting complexes: multiple activators and wide range of substrates might keep APC perpetually busy. Cell Cycle **4**(8): 1084–1092

Ge L, Chen H, Jiang J-F, Zhao Y, Xu M-L, Xu Y-Y, Tan K-H, Xu Z-H, Chong K (2004) Overexpression of *OsRAA1* causes pleiotropic phenotypes in transgenic rice plants, including altered leaf, flower, and root development and root response to gravity. Plant Physiol **135**(3): 1502–1513

Glickman MH, Ciechanover A (2002) The ubiquitin-proteasome proteolytic pathway: destruction for the sake of construction. Physiol Rev **82**(2): 373–428

Gu F, Bringmann M, Combs JR, Yang J, Bergmann DC, Nielsen E (2016) Arabidopsis CSLD5 functions in cell plate formation in a cell cycle-dependent manner. Plant Cell **28**(7): 1722–1737

Guo L, Jiang L, Zhang Y, Lu XL, Xie Q, Weijers D, Liu CM (2016) The anaphase-promoting complex initiates zygote division in Arabidopsis through degradation of cyclin B1. Plant J **86**(2): 161–174

Gutmann B, Gobert A, Giegé P (2012) PRORP Proteins support RNase P activity in both organelles and the nucleus in *Arabidopsis*. Genes Dev **26**(10): 1022–1027

Han Y, Cao H, Jiang J, Xu Y, Du J, Wang X, Yuan M, Wang Z, Xu Z, Chong K, et al. (2008) Rice ROOT ARCHITECTURE ASSOCIATED1 binds the proteasome subunit RPT4 and is degraded in a D-box and proteasome-dependent manner. Plant Physiol **148**(2): 843–855

He J, Chao WC, Zhang Z, Yang J, Cronin N, Barford D (2013) Insights into degron recognition by APC/C coactivators from the structure of an Acm1-Cdh1 complex. Mol. Cell **50**(5): 649–660

Hershko A, Ciechanover A (1998) The ubiquitin system. Annu Rev Biochem **67**(1): 425–479

Heyman J, Cools T, Canher B, Shavialenka S, Traas J, Vercauteren I, Van den Daele H, Persiau G, De Jaeger G, Sugimoto K, et al. (2016) The heterodimeric transcription factor complex ERF115-PAT1 grants regeneration competence. Nat Plants **2**(11): 16165

Heyman J, Cools T, Vandenbussche F, Heyndrickx KS, Van Leene J, Vercauteren I, Vanderauwera S, Vandepoele K, De Jaeger G, Van Der Straeten D, et al. (2013) ERF115 Controls root quiescent center cell division and stem cell replenishment. Science **342**(6160): 860–863

Heyman J, De Veylder L (2012) The anaphase-promoting complex/cyclosome in control of plant development. Mol Plant **5**(6): 1182–1194

Heyman J, Polyn S, Eekhout T, De Veylder L (2017) Tissue-specific control of the endocycle by the anaphase promoting Complex/cyclosome inhibitors UVI4 and DEL1. Plant Physiol **175**(1): 303–313

Heyman J, Van den Daele H, De Wit K, Boudolf V, Berckmans B, Verkest A, Lessa Alvim Kamei C, De Jaeger G, Koncz C, De Veylder L (2011) *Arabidopsis* ULTRAVIOLET-B-INSENSITIVE4 maintains cell division activity by temporal inhibition of the anaphase-promoting complex/cyclosome. Plant Cell **23**(12): 4394–4410

Houbaert A, Zhang C, Tiwari M, Wang K, de Marcos Serrano A, Savatin DV, Urs MJ, Zhiponova MK, Gudesblat GE, Vanhoutte I, et al. (2018) POLAR-guided signalling complex assembly and localization drive asymmetric cell division. Nature **563**(7732): 574–578

Ishizaki K, Nishihama R, Ueda M, Inoue K, Ishida S, Nishimura Y, Shikanai T, Kohchi T (2015) Development of gateway binary vector series with four different selection markers for the liverwort *Marchantia polymorpha*. PLoS ONE **10**(9): e0138876

Johnson M, Zaretskaya I, Raytselis Y, Merezhuk Y, McGinnis S, Madden TL (2008) NCBI BLAST: a better web interface. Nucleic Acids Res **36**(Web Server issue): W5–W9

Juraniec M, Heyman J, Schubert V, Salis P, De Veylder L, Verbruggen N (2016) Arabidopsis *COPPER MODIFIED RESISTANCE1/PATRONUS1* is essential for growth adaptation to stress and required for mitotic onset control. New Phytol **209**(1): 177–191

Karimi M, Bleys A, Vanderhaeghen R, Hilson P (2007) Building blocks for plant gene assembly. Plant Physiol **145**(4): 1183–1191

Karimi M, De Meyer B, Hilson P (2005) Modular cloning in plant cells. Trends Plant Sci **10**(3): 103–105

Karimi M, Inzé D, Depicker A (2002) GATEWAY^{TM} Vectors for *Agrobacterium*-mediated plant transformation. Trends Plant Sci **7**(5): 193–195

Kasili R, Walker JD, Simmons LA, Zhou J, De Veylder L, Larkin JC (2010) SIAMESE Cooperates with the CDH1-like protein CCS52A1 to establish endoreplication in *Arabidopsis thaliana* trichomes. Genetics **185**(1): 257–268

Kevei Z, Baloban M, Da Ines O, Tiricz H, Kroll A, Regulski K, Mergaert P, Kondorosi E (2011) Conserved CDC20 cell cycle functions are carried out by two of the five isoforms in *Arabidopsis thaliana*. PLoS One **6**(6): e20618

Kheibarshekan Asl L, Dhondt S, Boudolf V, Beemster GTS, Beeckman T, Inzé D, Govaerts W, De Veylder L (2011) Model-based analysis of Arabidopsis leaf epidermal cells reveals

distinct division and expansion patterns for pavement and guard cells. Plant Physiol **156**(4): 2172–2183

Kubota A, Ishizaki K, Hosaka M, Kohchi T (2013) Efficient *Agrobacterium*-mediated transformation of the liverwort *Marchantia polymorpha* using regenerating thalli. Biosci Biotechnol Biochem **77**(1): 167–172

Kwee H-S, Sundaresan V (2003) The *NOMEGA* gene required for female gametophyte development encodes the putative APC6/CDC16 component of the anaphase promoting Complex in *Arabidopsis*. Plant J **36**(6): 853–866

Lammens T, Boudolf V, Kheibarshekan L, Zalmas LP, Gaamouche T, Maes S, Vanstraelen M, Kondorosi E, La Thangue NB, Govaerts W, et al. (2008) Atypical E2F activity restrains APC/$C^{CCS52A2}$ function obligatory for endocycle onset. Proc Natl Acad Sci U S A **105**(38): 14721–14726

Larson-Rabin Z, Li Z, Masson PH, Day CD (2009) *FZR2/CCS52A1* expression is a determinant of endoreduplication and cell expansion in Arabidopsis. Plant Physiol **149**(2): 874–884

Lei Y, Lu L, Liu H-Y, Li S, Xing F, Chen L-L (2014) CRISPR-P: a web tool for synthetic single-guide RNA design of CRISPR-system in plants. Mol Plant **7**(9): 1494–1496

Li D, Flores-Sandoval E, Ahtesham U, Coleman A, Clay JM, Bowman JL, Chang C (2020) Ethylene-independent functions of the ethylene precursor ACC in *Marchantia polymorpha*. Nat Plants **6**(11): 1335–1344

Lin Q, Wang D, Dong H, Gu S, Cheng Z, Gong J, Qin R, Jiang L, Li G, Wang JL, et al. (2012) Rice APC/C^{TE} controls tillering by mediating the degradation of MONOCULM 1. Nat Commun **3**: 752

Lin Q, Wu F, Sheng P, Zhang Z, Zhang X, Guo X, Wang J, Cheng Z, Wang J, Wang H, et al. (2015) The SnRK2-APC/C^{TE} regulatory module mediates the antagonistic action of gibberellic acid and abscisic acid pathways. Nat Commun **6**: 7981

Lin Q, Zhang Z, Wu F, Feng M, Sun Y, Chen W, Cheng Z, Zhang X, Ren Y, Lei C, et al. (2020) The APC/C^{TE} E3 ubiquitin ligase complex mediates the antagonistic regulation of root growth and tillering by ABA and GA. Plant Cell **32**(6): 1973–1987

Liu Y, Ye W, Li B, Zhou X, Cui Y, Running MP, Liu K (2012) CCS52A2/FZR1, A cell cycle regulator, is an essential factor for shoot apical meristem maintenance in *Arabidopsis thaliana*. BMC Plant Biol **12**: 135

Marrocco K, Criqui M-C, Zervudacki J, Schott G, Eisler H, Parnet A, Dunoyer P, Genschik P (2012) APC/C-mediated degradation of dsRNA-binding protein 4 (DRB4) involved in RNA silencing. PLoS One **7**(4): e35173

Mesrian Tanha H, Mojtabavi Naeini M, Rahgozar S, Rasa SMM, Vallian S (2015) Modified tetra-primer ARMS PCR as a single-nucleotide polymorphism genotyping tool. Genet Test Mol Biomark **19**(3): 156–161

Ogawa D, Abe K, Miyao A, Kojima M, Sakakibara H, Mizutani M, Morita H, Toda Y, Hobo T, Sato Y, et al. (2011) RSS1 Regulates the cell cycle and maintains meristematic activity under stress conditions in rice. Nat Commun **2**: 278

Ossowski S, Schneeberger K, Clark RM, Lanz C, Warthmann N, Weigel D (2008) Sequencing of natural strains of *Arabidopsis thaliana* with short reads. Genome Res **18**(12): 2024–2033

Peters J-M (2002) The anaphase-promoting complex: proteolysis in mitosis and beyond. Mol Cell **9**(5): 931–943

Pfleger CM, Kirschner MW (2000) The KEN box: an APC recognition signal distinct from the D box targeted by Cdh1. Genes Dev **14**(6): 655–665

Proost S, Van Bel M, Vaneechoutte D, Van de Peer Y, Inzé D, Mueller-Roeber B, Vandepoele K (2015) PLAZA 3.0: an access point for plant comparative genomics. Nucleic Acids Res **43**(Database issue): D974–D981

Qin L, Guimarães DSPSF, Melesse M, Hall MC (2016) Substrate recognition by the Cdh1 destruction box receptor is a general requirement for APC/C^{Cdh1}-mediated proteolysis. J Biol Chem **291**(30): 15564–15574

Rojas CA, Eloy NB, Lima MDF, Rodrigues RL, Franco LO, Himanen K, Beemster GTS, Hemerly AS, Ferreira PCG (2009) Overexpression of the *Arabidopsis* anaphase promoting complex subunit *CDC27a* increases growth rate and organ size. Plant Mol. Biol **71**(3): 307–318

Saint-Marcoux D, Proust H, Dolan L, Langdale JA (2015) Identification of reference genes for real-time quantitative PCR experiments in the liverwort *Marchantia polymorpha*. PLoS One **10**(3): e0118678

Sauret-Güeto S, Frangedakis E, Silvestri L, Rebmann M, Tomaselli M, Markel K, Delmans M, West A, Patron NJ, Haseloff J, et al. (2020) Systematic tools for reprogramming plant gene expression in a simple model, *Marchantia polymorpha*. ACS Synth. Biol **9**(4): 864–882

Shimada TL, Shimada T, Hara-Nishimura I (2010) A rapid and non-destructive screenable marker, FAST, for identifying transformed seeds of *Arabidopsis thaliana*. Plant J **61**(3): 519–528

Smertenko AP, Kaloriti D, Chang HY, Fiserova J, Opatrny Z, Hussey PJ (2008) The C-terminal variable region specifies the dynamic properties of Arabidopsis microtubule-associated protein MAP65 isotypes. Plant Cell **20**(12): 3346–3358

Sun H, Schneeberger K (2015) SHOREmap v3.0: fast and accurate identification of causal mutations from forward genetic screens. Methods Mol. Biol **1284**: 381–395

Tarayre S, Vinardell JM, Cebolla A, Kondorosi A, Kondorosi E (2004) Two classes of the Cdh1-type activators of the anaphase-promoting complex in plants: novel functional domains and distinct regulation. Plant Cell **16**(2): 422–434

Truernit E, Bauby H, Dubreucq B, Grandjean O, Runions J, Barthelemy J, Palauqui JC (2008) High-resolution whole-mount imaging of three-dimensional tissue organization and gene expression enables the study of phloem development and structure in Arabidopsis. Plant Cell **20**(6): 1494–1503

Ursache R, Andersen TG, Marhavý P, Geldner N (2018) A protocol for combining fluorescent proteins with histological stains for diverse cell wall components. Plant J **93**(2): 399–412

Van Bel M, Diels T, Vancaester E, Kreft L, Botzki A, Van de Peer Y, Coppens F, Vandepoele K (2018) PLAZA 4.0: an integrative resource for functional, evolutionary and comparative plant genomics. Nucleic Acids Res **46**(D1): D1190–D1196

Vaneechoutte D, Vandepoele K (2019) Curse: building expression atlases and co-expression networks from public RNA-Seq data. Bioinformatics **35**(16): 2880–2881

Vanstraelen M, Baloban M, Da Ines O, Cultrone A, Lammens T, Boudolf V, Brown SC, De Veylder L, Mergaert P, Kondorosi E (2009) APC/C^{CCS52A} complexes control meristem maintenance in the *Arabidopsis* root. Proc Natl Acad Sci U S A **106**(28): 11806–11811

Wang Y, Hou Y, Gu H, Kang D, Chen Z, Liu J, Qu L-J (2012) The Arabidopsis APC4 subunit of the anaphase-promoting complex/cyclosome (APC/C) is critical for both female gametogenesis and embryogenesis. Plant J **69**(2): 227–240

Wang Y, Hou Y, Gu H, Kang D, Chen Z-L, Liu J, Qu L-J (2013) The *Arabidopsis* anaphase-promoting complex/cyclosome subunit 1 is critical for both female gametogenesis and embryogenesis J. Integr. Plant Biol **55**(1): 64–74

Westermann J, Koebke E, Lentz R, Hülskamp M, Boisson-Dernier A (2020) A comprehensive toolkit for quick and easy visualization of marker proteins, protein-protein interactions and cell morphology in *Marchantia polymorpha*. Front. Plant Sci **11**: 569194

Willems A, De Veylder L (2022) The plant anaphase-promoting complex/cyclosome. Annu Rev Cell Dev Biol **38**: 25–48

Willems A, Heyman J, Eekhout T, Achon I, Pedroza-Garcia JA, Zhu T, Li L, Vercauteren I, Van den Daele H, van de Cotte B, et al. (2020) The cyclin CYCA3; 4 is a postprophase target of the APC/$C^{CCS52A2}$ E3-ligase controlling formative cell divisions in Arabidopsis. Plant Cell **32**(9): 2979–2996

Xu Y, Cao H, Chong K (2010) APC-targeted RAA1 degradation mediates the cell cycle and root development in plants. Plant Signal. Behav **5**(3): 218–223

Xu Y, Jin W, Li N, Zhang W, Liu C, Li C, Li Y (2016) UBIQUITIN-SPECIFIC PROTEASE14 interacts with ULTRAVIOLET-B INSENSITIVE4 to regulate endoreduplication and cell and organ growth in Arabidopsis. Plant Cell **28**(5): 1200–1214

Xu C, Wang Y, Yu Y, Duan J, Liao Z, Xiong G, Meng X, Liu G, Qian Q, Li J, et al. (2012) Degradation of MONOCULM 1 by APC/C^{TAD1} regulates rice tillering. Nat Commun **3**: 750

Yang W, Wightman R, Meyerowitz EM (2017) Cell cycle control by nuclear sequestration of *CDC20* and *CDH1* mRNA in plant stem cells. Mol. Cell **68**(6): 1108–1119

Zheng B, Chen X, McCormick S (2011) The anaphase-promoting complex is a dual integrator that regulates both microRNA-mediated transcriptional regulation of *Cyclin B1* and degradation of cyclin B1 during *Arabidopsis* male gametophyte development. Plant Cell **23**(3): 1033–1046

Zhong S, Xu Y, Yu C, Zhang X, Li L, Ge H, Ren G, Wang Y, Ma J, Zheng Y, et al. (2019) Anaphase-promoting complex/cyclosome regulates RdDM activity by degrading DMS3 in *Arabidopsis*. Proc Natl Acad Sci U S A **116**(9): 3899–3908

Zhou Z, He M, Shah AA, Wan Y (2016) Insights into APC/C: from cellular function to diseases and therapeutics. Cell Div **11**: 9